Characterization of an Intracavity Optical Parametric Oscillator

DANIEL SANDBERG

FOI-R-- 1737 --SE Technical report
ISSN 1650-1942 September 2005

Sensor Technology

FOI is an assignment-based authority under the Ministry of Defence. The core activities are research, method and technology development, as well as studies for the use of defence and security. The organization employs around 1350 people of whom around 950 are researchers. This makes FOI the largest research institute in Sweden. FOI provides its customers with leading expertise in a large number of fields such as security-policy studies and analyses in defence and security, assessment of different types of threats, systems for control and management of crises, protection against and management of hazardous substances, IT-security an the potential of new sensors.

FOI
Defence Research Agency
Sensor Technology
P.O. Box 1165
SE-581 11 Linköping

Phone: +46 13 37 80 00
Fax: +46 13 37 81 00

www.foi.se

Characterization of an Intracavity Optical Parametric Oscillator

FOI-R--1737--SE
ISSN 1650-1942

Sensor Technology
Technical report

September 2005

Issuing organization
FOI – Swedish Defence Research Agency
Sensor Technology
P.O. Box 1165
SE-581 11 Linköping

Report number, ISRN
FOI-R--1737--SE

Report type
Technical report

Research area code
6. Electronic Warfare and deceptive measures

Month year
September 2005

Project no.
E3020

Sub area code
61 Electronic Warfare including Electromagnetic Weapons and Protection

Sub area code 2

Author/s (editor/s)
Daniel Sandberg

Project manager
Lars Sjöqvist

Approved by
Ove Steinvall

Sponsoring agency
HKV

Scientifically and technically responsible
Lars Sjöqvist/Markus Henriksson

Report title
Characterization of an Intracavity Optical Parametric Oscillator

Abstract (not more than 200 words)
The wavelength of laser radiation can be converted by using nonlinear optical crystals. One nonlinear process is parametric oscillation where a fundamental wavelength is converted into two longer wavelengths. In this work the possibilities to build a stable source producing radiation in the 2 μm wavelength region was investigated. This radiation can, in further conversion processes, generate longer wavelengths with applications in e.g. laser countermeasures and laser for atmospheric remote sensing. An intracavity Optical Parametric Oscillator (OPO) using the nonlinear crystal $KTiOPO_4$ (KTP) was designed to convert pulsed Nd:YAG laser radiation operating at 1064 nm wavelength to regions around 2 μm. The maximum converted output power achieved for an intracavity OPO configuration was 2.5 W using a Nd:YAG output power of 20 W. An analysis of thermal lensing of the laser rod and the influence from thermal effects on output power from the system was carried out.

Keywords
Laser, OPO, thermal effects, wavelength conversion

Further bibliographic information

Language English

ISSN 1650-1942

Pages 75 p.

Price acc. to pricelist

Utgivare
FOI - Totalförsvarets forskningsinstitut
Sensorteknik
Box 1165
581 11 Linköping

Rapportnummer, ISRN
FOI-R--1737--SE

Klassificering
Teknisk rapport

Forskningsområde
6. Telekrig och vilseledning

Månad, år
September 2005

Projektnummer
E3020

Delområde
61 Telekrigföring med EM-vapen och skydd

Delområde 2

Författare/redaktör
Daniel Sandberg

Projektledare
Lars Sjöqvist

Godkänd av
Ove Steinvall

Uppdragsgivare/kundbeteckning
HKV

Tekniskt och/eller vetenskapligt ansvarig
Lars Sjöqvist/Markus Henriksson

Rapportens titel (i översättning)
Karakterisering av en optisk parametrisk oscillator

Sammanfattning (högst 200 ord)
Laserstrålning kan konverteras genom att använda icke-linjära optiska kristaller. En icke-linjär process är parametrisk oscillering, där en fundamental våglängd kan konverteras till två nya längre våglängder. I det här arbetet undersöktes möjligheterna att konstruera en stabil källa som producerar våglängder runt 2 µm. Strålningen kan i ytterligare steg användas för vidare konvertering till längre våglängder med användningsområden inom t.ex. laserbaserade motmedel och laser för fjärranalys av atmosfären. En optisk parametrisk oscillator (OPO) med en intrakavitetskonfiguration utformades genom att använda den ickelinjära kristallen $KTiOPO_4$ (KTP) för att konvertera pulsad Nd:YAG laserstrålning vid 1064 nm till ett våglängdsområde kring 2 µm. Den maximalt konverterade effekten för en intrakavitets OPO-konfiguration var 2,5 W vid en Nd:YAG effekt på 20 W. En analys av den termiska linsen i laserstaven och termiska effekters påverkan på systemets uteffekt studerades.

Nyckelord
Laser, OPO, termiska effekter, våglängdskonvertering

Övriga bibliografiska uppgifter

Språk Engelska

ISSN 1650-1942

Antal sidor: 75 s.

Distribution enligt missiv

Pris: Enligt prislista

Contents

Chapter 1

Introduction

Nonlinear optics is an interesting research field with many applications. As the development of lasers quickly advanced since its introduction in the 1960s, the development of nonlinear optics also progressed. This was due to the fact that laser beams had high energy densities necessary to produce nonlinear effects. Another important step was the progress in the fabrication of high quality optical nonlinear materials.

The main advantage of using nonlinear optical materials is the possibility to generate specific wavelengths from the fundamental wavelength of the laser. One of the most basic techniques is to double the frequency of the radiation. Another process is optical parametric oscillation (OPO), in which a light beam at one frequency generates two beams at lower frequencies, when propagating through the nonlinear material. By rotating the crystal relative to the incident beam, a spectrum of laser radiation can be generated. This wavelength selectivity makes the OPO interesting in a number of applications such as spectroscopy, medical research, display technology, environmental monitoring and light detection and ranging (LIDAR).

1.1 Scope of work

The purpose of this study is to perform an analysis of an intracavity optical parametric oscillator, converting Nd:YAG radiation at $\lambda = 1.064\,\mu$m to regions around $\lambda = 2\,\mu$m using the nonlinear crystal Potassium Titanyl Phosphate, $KTiOPO_4$, commonly denoted KTP.

Measurements of converted output power and pulse and output power stability have been performed. Investigations of thermal effects, such as thermal lensing of the laser rod and output power fluctuations due to instabilities, are included in this study. Labview and Matlab have been used to develop programs for measurement and theoretical calculations.

The experiments were performed using a two-mirror pump-resonator setup with an intracavity resonator for the KTP crystal. All mirrors used in the experiments

were plane. More elaborate setups such as ring and bow-tie resonators have not been investigated in this study.

Chapter 2

Theory

2.1 Basic Laser Theory

When light is absorbed, or emitted, a transfer between energy levels takes place. The fundamental theory behind lasing action was established as early as 1916 by Albert Einstein, when he predicted the existence of a special radiative process called *stimulated emission*. The first operable laser made out of pink ruby, was invented by the physicist Theodore Harold Maiman in 1960 [1]. The word laser itself is an acronym that stands for **L**ight **A**mplification by **S**timulated **E**mission of **R**adiation and a laser system contains three essential elements, the pump, the optical gain medium and the resonator.

Laser radiation can be characterized by being *monochromatic*, i.e. the radiation generated is of a single wavelength, *directional* which means that the beam has very little divergence compared to normal light. It is also extremely *coherent*, which means that the photons generated have the same direction, same polarization, same phase and same spectral characteristics.

According to Einstein the interaction with light and matter can be described by three processes: stimulated absorption, spontaneous emission and stimulated emission.

2.1.1 Radiative Processes

Let us consider a material with two non-degenerate levels, and that the levels are perfectly discrete, see figure 2.1. The total number of atoms in the two levels are also considered to be constant in time.

Stimulated Absorption, can symbolically be written as

$$atom + photon \rightarrow atom^*$$

where $atom^*$ denotes the excited atom. Absorption is the process where an atom absorbs a photon from an external field and the population of the energy level E_1 will decrease.

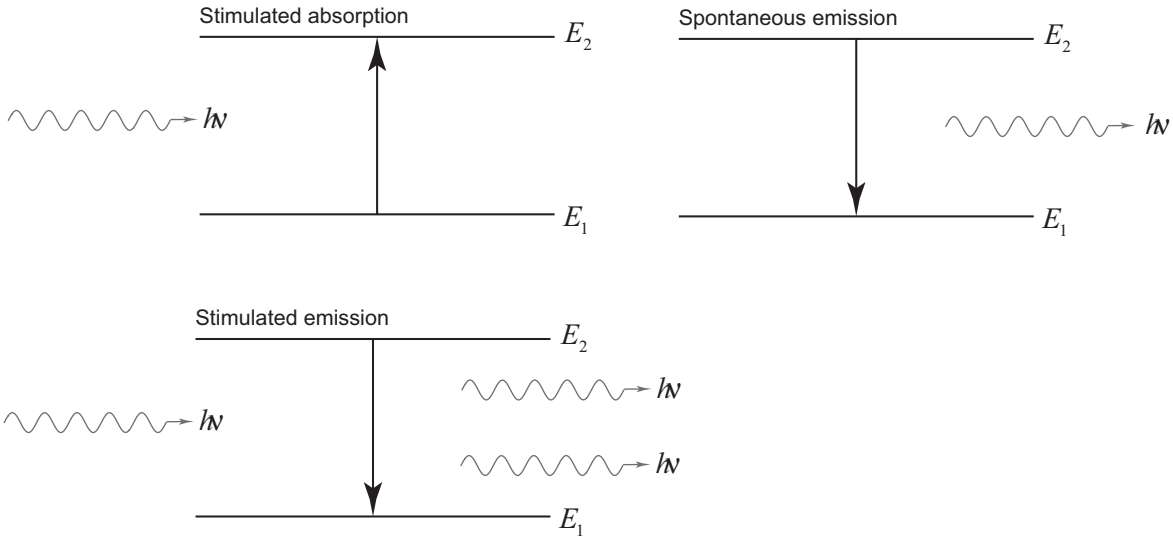

Figure 2.1. Interaction of radiation.

Spontaneous Emission, can be represented as

$$atom^* \rightarrow atom + photon.$$

It is the process that describes the spontaneous decay from atoms at the energy level E_2 to E_1, adding photons with energy $E_2 - E_1 = h\nu$ to the radiation field.

Stimulated Emission, can be written:

$$atom^* + photon \rightarrow atom + 2photons.$$

This is the reverse process of absorption. The atom gives up excess energy to the field by induced emission, adding coherently to the intensity. This means that the added photon has the same frequency, phase and polarization, and propagates in the same direction to the field that induced this transition.

The Nd:YAG laser belongs to the class of 4-level laser systems and for a more detailed description regarding inversion and lasing, see appendix A.

2.2 Optical resonators

An important part in the laser system is the resonator. To amplify the field, the laser medium is put inside a cavity that allows the EM-wave to bounce back and forth. The wave will resonate if the length of the cavity is an integral multiple of half the wavelength $L = \frac{m\lambda}{2}$ [2]. In a general system, many longitudinal modes fulfil this requirement, leading to multi-mode resonance in the cavity. The number of modes with sufficient gain to oscillate, is determined from the linewidth of the laser transition [3]. The linewidth arise from the fact that the transition levels never are perfectly discrete in figure 2.1, rather a function describing the response to EM-waves at different frequencies.

In each round-trip there is amplification gain, see figure 2.2. There are also different losses from diffraction, imperfections in the rod, absorption in mirrors etc. within the cavity. Lasing will begin when the gain is greater than the these losses. Let g be the gain per unit length, α the losses and l the length of the rod. In each passage the intensity will gain a factor $\exp((g-\alpha)l)$ so the threshold must be [3]

$$\begin{aligned} &G = R_1 R_2 \exp(2l(g-\alpha)) = 1 \\ &R_1, R_2 \text{ mirror reflectivities.} \\ &g \propto \Delta N \end{aligned} \tag{2.1}$$

where ΔN is the difference in population between the levels, where the lasing

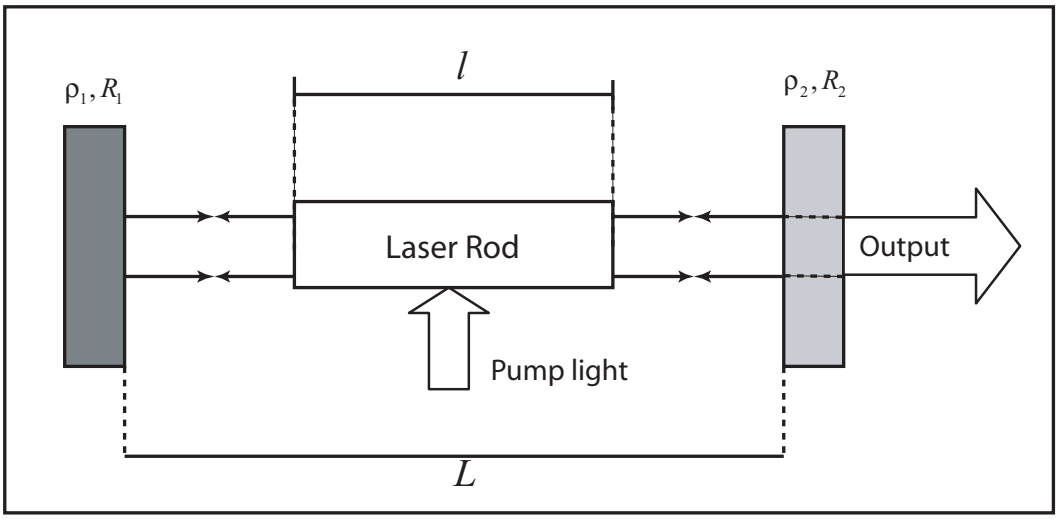

Figure 2.2. Optical cavity with reflectivities $R_1 = 100\%$, $R_2 < 100\%$ and curvatures ρ_1, ρ_2.

takes place.

If $G > 1$ the intensity will grow in each round-trip and will be infinite according to equation (2.1). This is prevented by the *gain saturation* which means that the gain factor is decreased as the intensity of the radiation is increased due to depletion of the inversion. Steady state is reached when the left hand side in equation (2.1) equals one.

2.2.1 Q-switching

An important part in laser systems is to be able to pulse the system. This is achieved by a technique called Q-switching or Q-spoiling. When using a Q-switch, a physical alteration is done to the feedback in the cavity, in which large losses are introduced, increasing the threshold so that lasing is prevented. The inversion during this time increases and reaches a level beyond the normal required threshold resulting in an increase in stored energy in energy level two, see figure A.1 appendix A. At maximum population inversion, the system is "reset" causing it to lase again

by now releasing its stored energy in one pulse. The development of this pulse can be followed in figure 2.3.

A perfect Q-switch should switch from one condition to the other as fast as possible causing minimal losses in the resonator when opened, and high losses in the resonator when shut.

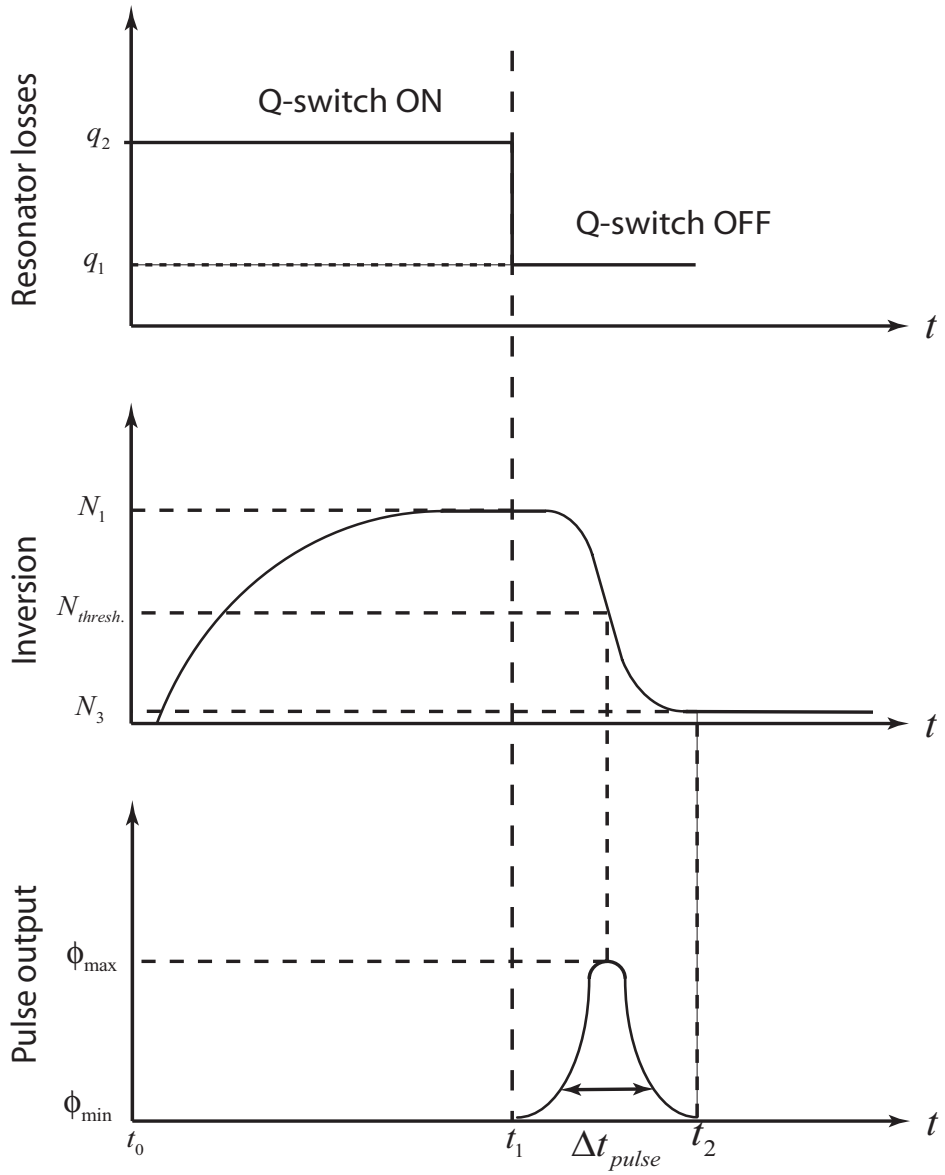

Figure 2.3. Pulse development using Q-switching showing losses, inversion buildup and pulse output.

2.3 Gaussian Beam propagation

2.3.1 Gaussian Beams

In the simplest mode, called the fundamental mode, the laser beam (considering the electric field) exhibits a transverse Gaussian irradiance distribution. To put it in another way, the cross section of a Gaussian beam has a transverse electric field distribution that follows a Gaussian profile. In higher order modes, this distribution is instead described by the so called *Hermite-Gaussian* functions. Understanding these modes are important, since in a stable cavity they form naturally because the modes "match" the mirrors, i.e. resonance is achieved for those higher order modes for a given stable laser cavity.

The complete description of the Gaussian field [2] in cartesian coordinates is

$$E(x,y,z) = E_{m,p} H_m\left[\frac{x}{\sqrt{2}w(z)}\right] H_p\left[\frac{y}{\sqrt{2}w(z)}\right] \times \frac{w_0}{w(z)} \exp\left[-\frac{x^2+y^2}{w^2(z)}\right] \times \exp\left[-j\left[kz - (1+m+p)\tan^{-1}\left(\frac{z}{z_R}\right)\right]\right] \times \exp\left[-j\frac{k(x^2+y^2)}{2R(z)}\right] \tag{2.2}$$

where H_m and H_p are the Hermite polynomials which can be generated from [4]

$$H_n(x) = (-1)^n e^{x^2} \frac{d^n}{dx^n} e^{-x^2}. \tag{2.3}$$

The Hermite-Gaussian modes are depicted in figure 2.4.

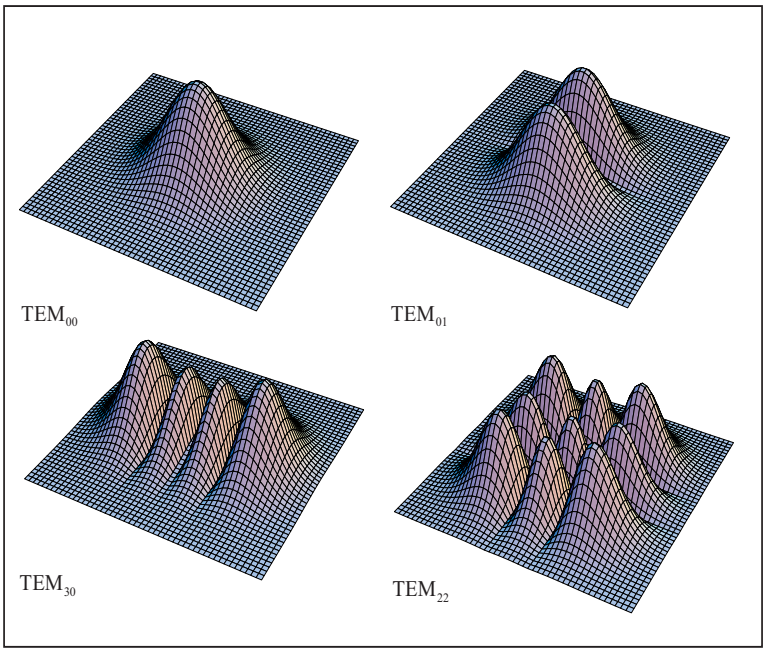

Figure 2.4. Intensity distributions for different orders of the Hermite-Gaussian modes from equation (2.2).

These eigensolutions can also be circular symmetric, and are then called Laguerre-Gaussian modes, consisting of Laguerre polynomials. Equation (2.2) is often referred to as the $\mathrm{TEM}_{m,p}$ mode, meaning **T**ransverse **E**lectric **M**agnetic, and the subscripts m and p are the order of the Hermite polynomials. These solutions form a complete and orthogonal set of functions, the simplest being the fundamental mode or gaussian beam denoted $\mathrm{TEM}_{0,0}$ described by

$$E(r,z) = E_0 \frac{w_0}{w(z)} \exp\left[-\frac{r^2}{w^2(z)}\right] \exp\left(-j\left[kz - \phi(z)\right]\right) \exp\left(-j\frac{kr^2}{2R(z)}\right) \qquad (2.4)$$
$$r^2 = x^2 + y^2.$$

The Gaussian Beam Parameters

The involved parameters from equation (2.2) are illustrated in figure 2.5.

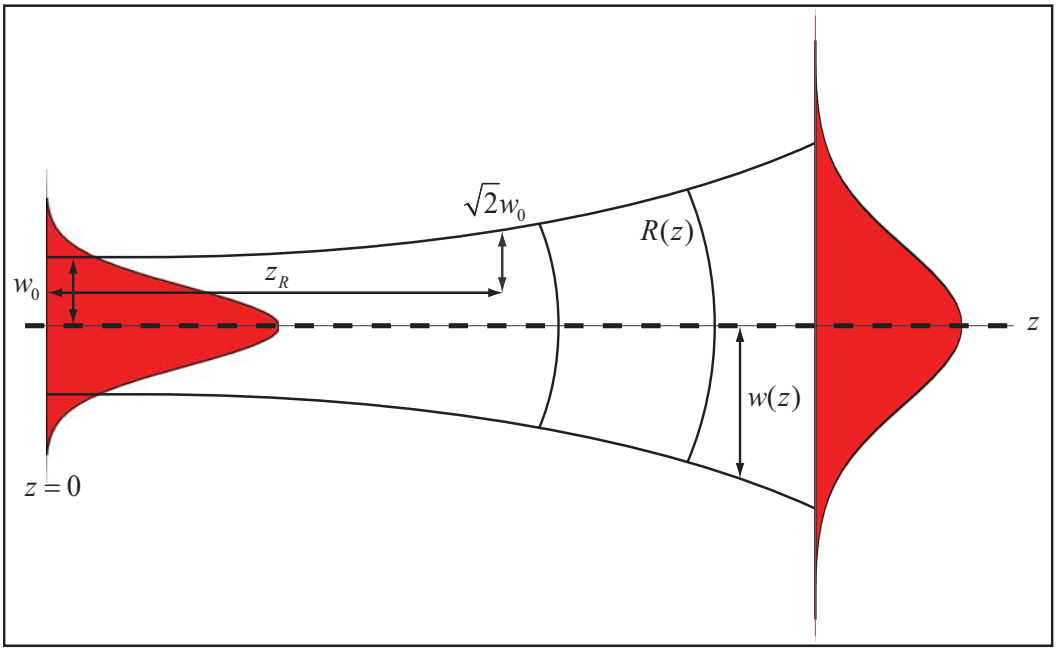

Figure 2.5. Gaussian Beam parameters also showing irradiance distribution change propagating a distance z.

The *Rayleigh length* is related to the wavelength, λ, and beam waist, w_0, according to [2]

$$z_R = \frac{\pi w_0^2}{\lambda}. \qquad (2.5)$$

The Rayleigh length describes the distance from w_0 to where the cross sectional area of the beam has doubled. As the distance from the waist location increases, the divergence of the beam naturally increases.

When propagating a distance z from the waist, the *beam radius* will change.

The relation describing this is [2]

$$w(z) = w_0\sqrt{1+\left(\frac{z}{z_R}\right)^2}. \tag{2.6}$$

Another important beam parameter is the *wavefront curvature*, which is related to the Rayleigh length according to [2]

$$R(z) = z + \frac{z_R^2}{z}. \tag{2.7}$$

Equation (2.7) specifies the curvature of the laser beam wavefront, at a distance z from the beam waist.

2.3.2 Propagation of modes

A Gaussian beam, as it propagates through an optical system, will remain a Gaussian beam except from its amplitude and the complex beam parameter $q(z)$, which can be shown [1] to be

$$\frac{1}{q(z)} = \frac{1}{R(z)} - j\frac{\lambda}{\pi w^2(z)}. \tag{2.8}$$

$R(z)$ and $w(z)$ were defined previously. This parameter describes both the size and the curvature of the gaussian beam as a function of z. Using the parameter in conjunction with the matrix method, see appendix B, it is possible to propagate Gaussian beams through optical elements in an optical system.

The relation between the ABCD law, see appendix B, and the complex beam parameter is given by [5]

$$q_2 = \frac{Aq_1 + B}{Cq_1 + D} \tag{2.9}$$

which relates the output complex parameter q_2 to the input complex parameter q_1 by the system matrix.

2.3.3 Stability and the G-parameters

In order for the resonator to be stable, the complex beam parameter in relation (2.8) is required to reproduce itself $q(z + 2L) = q(z)$ in one round-trip, meaning that both the beam shape and the phase must reproduce itself in one round-trip [2]. This makes the matrix formalism especially useful for analyzing the stability of a resonator.

Consider a two mirror resonator according to figure 2.6, separated by a distance L, with mirror curvatures ρ_1 and ρ_2. In a stable resonator configuration, the light rays are assumed to be confined within the system, and does not diverge away from the axis causing "spill" around the edges of the mirrors.

Using the ABCD law, a general matrix for this system can be derived from the equivalent lens waveguide [5]

$$\widetilde{M} = \begin{pmatrix} 2g_1g_2 - 1 & 2Lg_2 \\ \dfrac{(2g_1g_2)^2 - 1}{2Lg_2} & 2g_1g_2 - 1 \end{pmatrix} \tag{2.10}$$

with

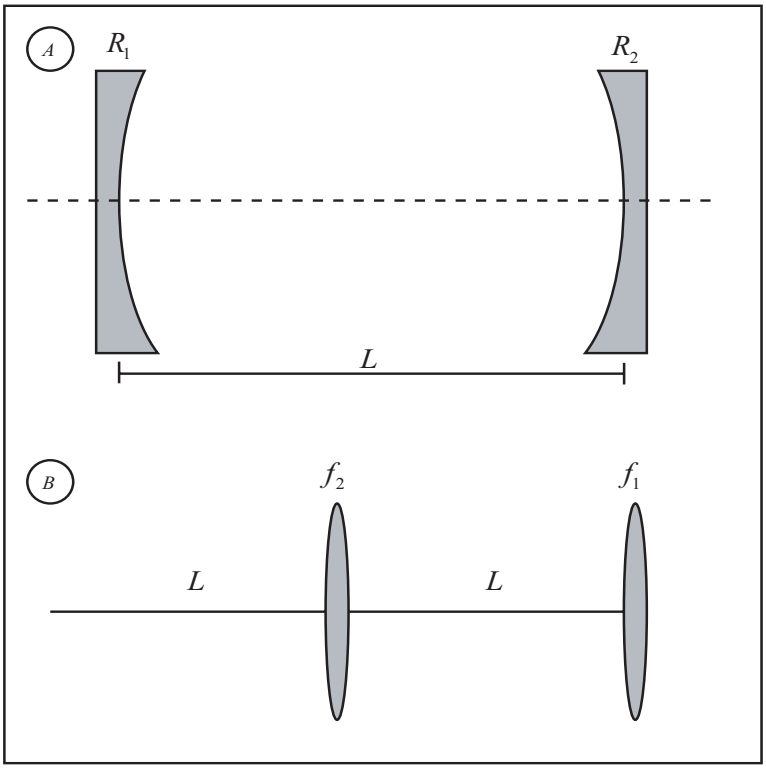

Figure 2.6. Resonator (A) and equivalent lens waveguide (B).

$$\begin{aligned} g_1 &= 1 - \frac{L}{\rho_1} \\ g_2 &= 1 - \frac{L}{\rho_2}. \end{aligned} \tag{2.11}$$

The condition for this resonator to be stable is [6]

$$-1 \leqslant \left(\frac{A+D}{2} \right) \leqslant 1 \tag{2.12}$$

or simply

$$0 \leqslant g_1 g_2 \leqslant 1. \tag{2.13}$$

If the relation 2.13 is plotted in the $g_1 g_2$ plane, see figure 2.7, different configurations of stable cavities can be analyzed from this figure.

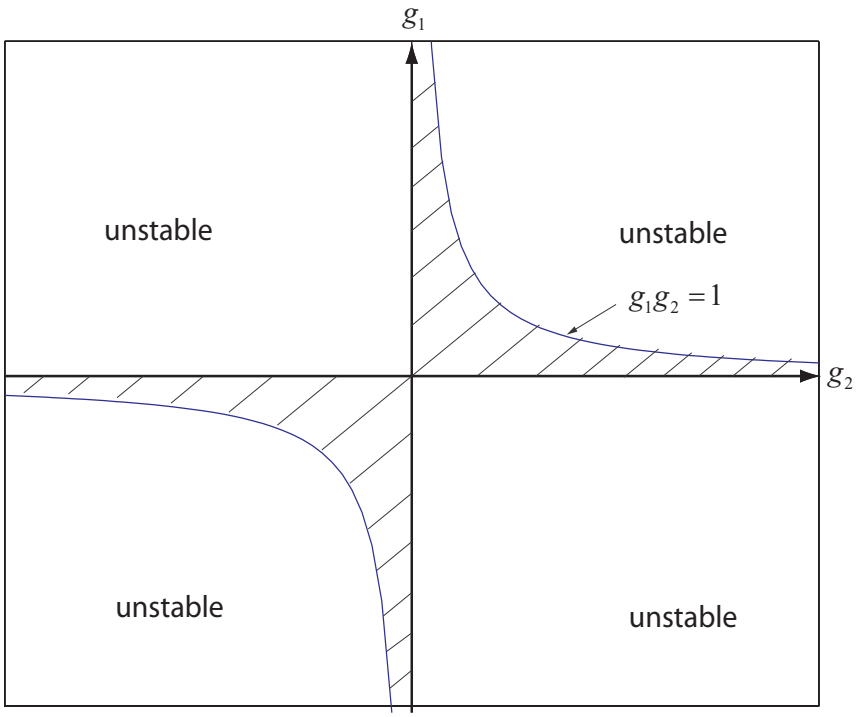

Figure 2.7. Stability diagram for the resonator in figure 2.6.

2.3.4 Resonators with internal lenses

A more complex resonator is shown in figure 2.8, with an internal lens with refractive power D. If the ABCD method is applied on this system, the transfer matrix will be [7]

$$\widetilde{M^*} = \begin{pmatrix} A & B \\ C & D \end{pmatrix} = \begin{pmatrix} 2g_1^*g_2^* - 1 + 2L^* \times g_2^*/\rho_1 & 2g_2^*L^* \\ AB/D & 2g_1^*g_2^* - 1 - 2L^* \times g_2^*/\rho_1 \end{pmatrix} \tag{2.14}$$

with the modified g-parameters and modified resonator length

$$\begin{aligned} g_i^* &= g_i - Dd_j\left(1 - \frac{d_i}{\rho_i}\right) \text{ for } i,j = 1,2; i \neq j \\ L^* &= d_1 + d_2 - Dd_1d_2 \\ D &= \frac{1}{f}, \text{ Refractive power of internal lens.} \end{aligned} \tag{2.15}$$

For a thick lens, the distances d_1 and d_2 are measured from the principal planes[1]

[1] Principal planes are hypothetical planes at which all the refraction are considered to happen.

of the lens, shown as h in figure 2.8.

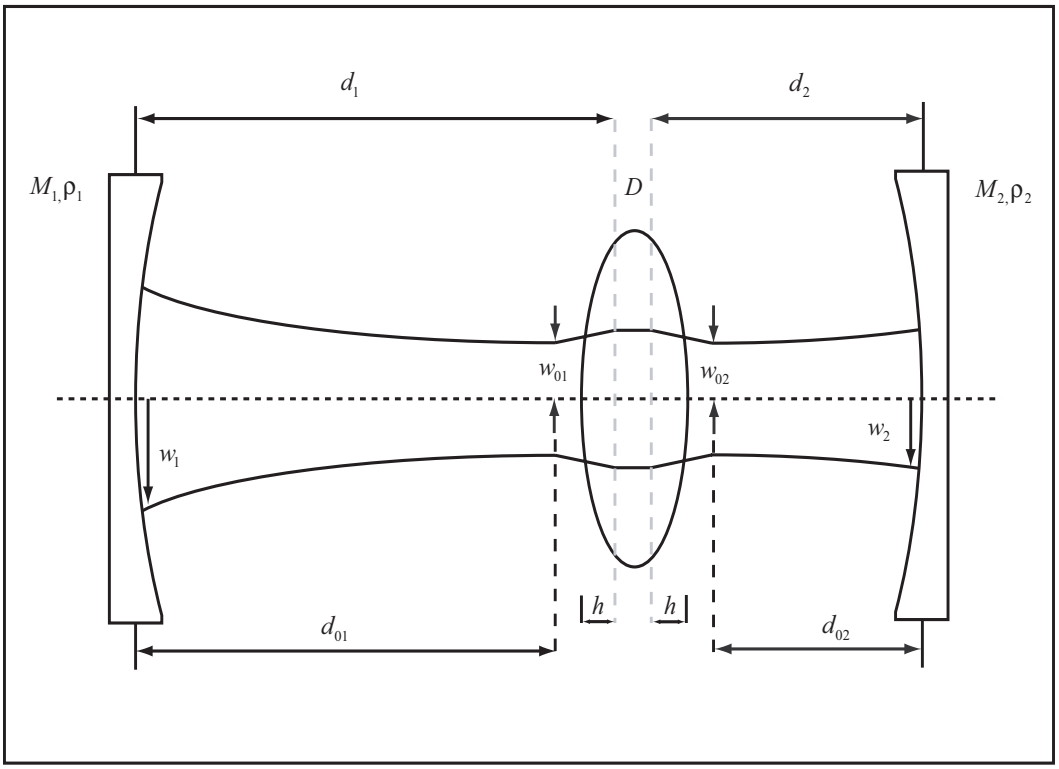

Figure 2.8. Resonator with an internal thick lens. Two internal waists w_{01} and w_{02} are located at distances d_{01} and d_{02}.

According to equation (2.15) the cavity equals an empty cavity but with modified length and mirror curvatures. The spot sizes on the mirrors for the $\mathrm{TEM}_{0,0}$ mode are the same for the equivalent resonator and the actual lens resonator. The beam waists however will be different. Depending on the mirror curvatures, the lens resonator can have two internal waists, w_{01} and w_{02}, as shown in figure 2.8. For the equivalent empty cavity, only one waist is present.

From equations (2.14) and (2.15), four refractive powers can be derived that intersects stability limits of the resonator in the modified stability diagram [7]

$$D_I = \frac{1}{d_1 - \rho_1} + \frac{1}{d_2 - \rho_2}, \text{ for } g_1^* g_2^* = 1, \; g_i^* > 0 \tag{2.16a}$$

$$D_{II} = \frac{1}{d_2} + \frac{1}{d_1 - \rho_1}, \text{ for } g_1^* = 0 \tag{2.16b}$$

$$D_{III} = \frac{1}{d_1} + \frac{1}{d_2 - \rho_2}, \text{ for } g_2^* = 0 \tag{2.16c}$$

$$D_{IV} = \frac{1}{d_1} + \frac{1}{d_2}, \text{ for } g_1^* g_2^* = 1, \; g_i^* < 0. \tag{2.16d}$$

The resonator with an internal lens will move along straight lines in the stability plot as D increases, as shown in figure 2.9. The slope of these lines depends on mirror curvatures and the position of the internal lens.

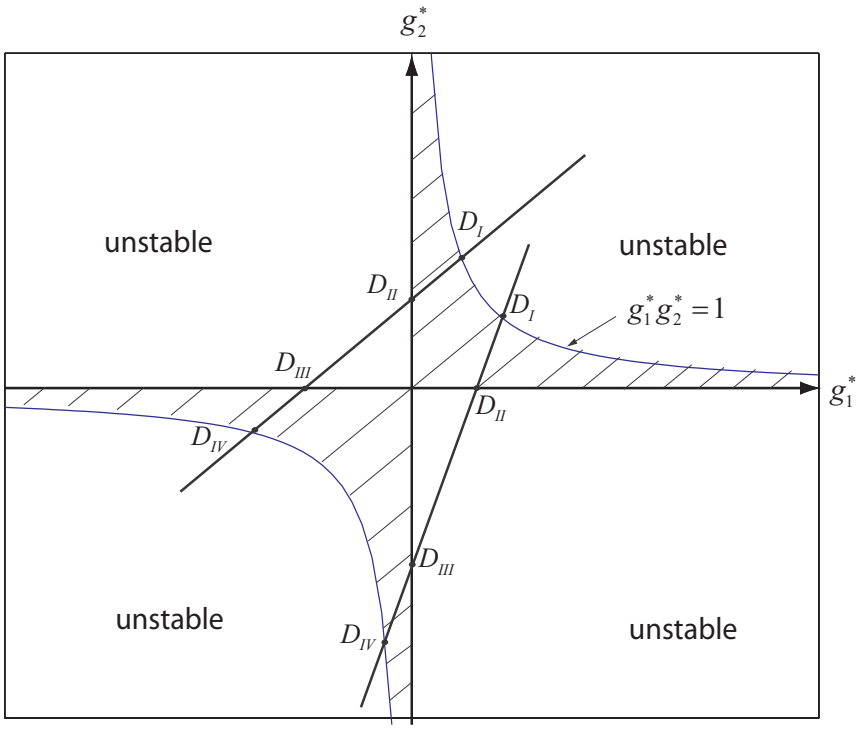

Figure 2.9. Stability diagram for resonator with an internal lens, showing the characteristic refractive powers.

2.4 Thermal lensing

When pumping the system, heat is uniformly absorbed in the volume of a circular symmetric Nd:YAG rod. Surface cooling makes the center hotter than the outer edges, which will introduce radial temperature gradients, illustrated in figure 2.10. These gradients will cause mechanical stresses and displacements in the rod. Inhomogeneous distribution of temperature and strain in the Nd:YAG material, will cause a change in refractive index at every point, and the result is that the rod itself will act as a thick lens, whose focal length varies with input power.

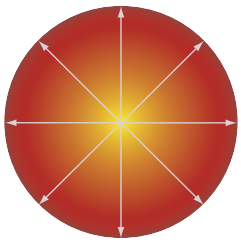

Figure 2.10. Drawing showing the cross section of a circular symmetric laser rod with thermal gradients.

A well established equation describing the refractive power is given by [3]

$$
\begin{aligned}
D &= \frac{P_a}{KA}\left(\frac{1}{2}\frac{dn}{dT} + \alpha C_{r,\phi} n_0^3 + \frac{\alpha r_0 (n_0 - 1)}{L}\right) \\
D &= \frac{1}{f}, \text{ Refractive power} \\
\frac{dn}{dT} &= \text{Temperature dependent change of the refractive index.} \\
K &= \text{Thermal Conductivity} \quad [\text{W m}^{-1}\text{K}^{-1}] \\
C_{r,\phi} &= \text{Photoelastic coefficient} \\
P_a &= \text{Total heat dissipated in the rod} \quad [\text{W}] \\
A &= \text{Cross sectional area of the rod} \quad [\text{m}^2] \\
L &= \text{Length of the rod} \quad [\text{m}] \\
n_0 &= \text{Refractive index} \\
r_0 &= \text{Radius of the rod} \quad [\text{m}] \\
\alpha &= \text{Thermal expansion} \quad [\text{K}^{-1}].
\end{aligned}
\tag{2.17}
$$

The refractive index is dependent on the polarization of the light, and in equation (2.17) there are two focal lengths, f_r, for all rays polarized in the radial direction and f_ϕ for rays in the tangential direction.

One method to reduce the lensing effect is to have the end faces of the rod slightly curved as illustrated in figure 2.11. Equation (2.17) needs to be modified by taking this into account[2]

$$
D = \frac{P_a}{KA}\left(\frac{1}{2}\frac{dn}{dT} + \alpha C_{r,\phi} n_0^3 + \frac{\alpha r_0 (n_0 - 1)}{L}\right) - \frac{2(n_0 - 1)}{\rho_0} \tag{2.18}
$$

where ρ_0 is the curvature of the end faces.

The total heat dissipated in the material is related to the electrical input power with an overall efficiency factor, describing how much that is actually absorbed as heat in the rod. This can be described by

$$
P_a = \eta V \times (I_p - I_{th}) \tag{2.19}
$$

where V is the laser driver voltage, I_p the pump current and I_{th} the threshold current for the pump diodes in the laser head. The factor η contains a number of efficiency parameters depending on the system. It also has different values during lasing action, and non-lasing conditions.

A plot of equation (2.18), varying the efficiency factor in (2.19) is shown in figure 2.12.

[2] Calculation is performed using thick lens geometry [1].

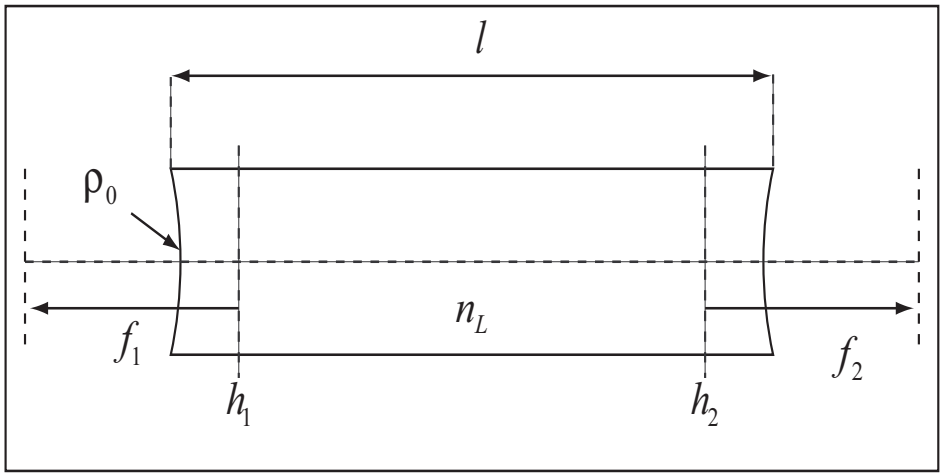

Figure 2.11. Laser rod with length l, curved end faces ρ_0, and principal planes h_1 and h_2. n_L is the refractive index of the material.

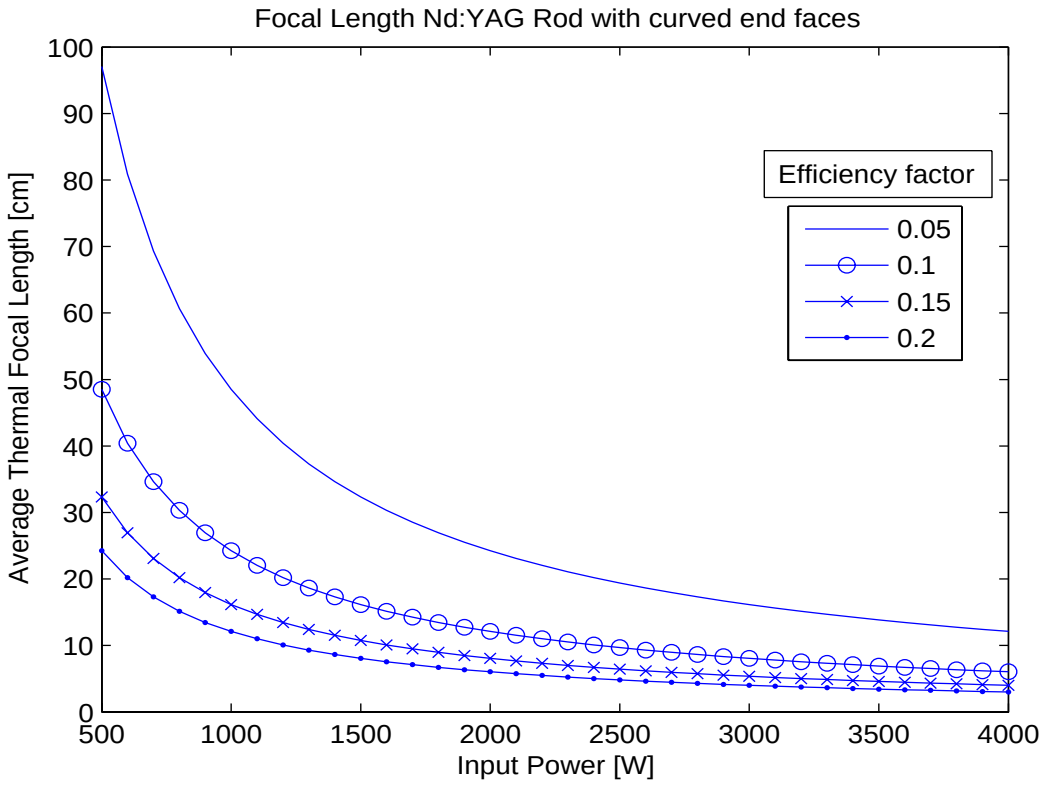

Figure 2.12. Theoretical calculation of the average focal lengths from equation (2.18), varying the efficiency factor η in equation (2.19). Constants were used considering Nd:YAG material.

2.5 Nonlinear Optics

2.5.1 Introduction to Nonlinear Optics

Consider a linear medium, where the polarization is described as

$$\mathbf{P} = \epsilon_0 \chi \mathbf{E}, \tag{2.20}$$

where

$$\chi^{(1)} = \frac{\epsilon}{\epsilon_0} - 1$$
$$\epsilon = \epsilon_r \epsilon_0 \tag{2.21}$$

is the linear *susceptibility* and ϵ_0 the *permittivity* of free space. Since the permittivity is in general given relative to that of vacuum, the actual permittivity is ϵ and ϵ_r the *dielectric constant*, which is material dependent.

When nonlinear effects are introduced, equation (2.20) needs to be expanded [8] according to

$$\mathbf{P} = \epsilon_0 \chi^{(1)} \mathbf{E} + \epsilon_0 \left(\chi^{(2)} \mathbf{EE} + \chi^{(3)} \mathbf{EEE} + \chi^{(4)} \mathbf{EEEE} \ldots \right) = \mathbf{P}^{\mathrm{L}} + \mathbf{P}^{\mathrm{NL}} \tag{2.22}$$

where $\chi^{(m)}, m = 1, 2, 3 \ldots$ now are tensors of the first, second, third rank etc. The strength of terms over two in the expansion will in general be considered weak, and therefore only second order processes are of interest here. The linear and nonlinear response are illustrated in figure 2.13.

Not all materials will provide second order nonlinear processes. Inversion symmetric media are materials with the following property

$$\widetilde{I}_{op} \mathbf{P} = -\mathbf{P}$$
$$\widetilde{I}_{op} \mathbf{E} = -\mathbf{E} \tag{2.23}$$

under some symmetry operator $\widetilde{I}_{op}$ [9]. When applying this operator on equation (2.22) this results in that all even orders of the tensors equals zero

$$\chi^{(2m)} = 0, \quad m = 1, 2, 3 \ldots \tag{2.24}$$

Effects from the second rank tensor are therefore only seen in noncentrosymmetric materials.

At high optical intensities the response of the medium will be nonlinear with the consequence that the nonlinear part of the polarization will induce new fields from the applied field.

2.5.2 Different Nonlinear processes

Consider a general field

$$E(\mathbf{r}, t) = \frac{1}{2} \left[E(\mathbf{r}, \omega) e^{(i(\mathbf{k} \cdot \mathbf{r} - \omega t))} + \text{c.c.} \right]. \tag{2.25}$$

Now assume a mixed field consisting of two frequency components

$$E(\mathbf{r}, t) = \frac{1}{2} \left[\mathbf{E}_1 e^{(i(\mathbf{k}_1 \cdot \mathbf{r} - \omega_1 t))} + \mathbf{E}_2 e^{(i(\mathbf{k}_2 \cdot \mathbf{r} - \omega_2 t))} + \text{c.c.} \right] \tag{2.26}$$

then using equation (2.22), the second order contribution will be

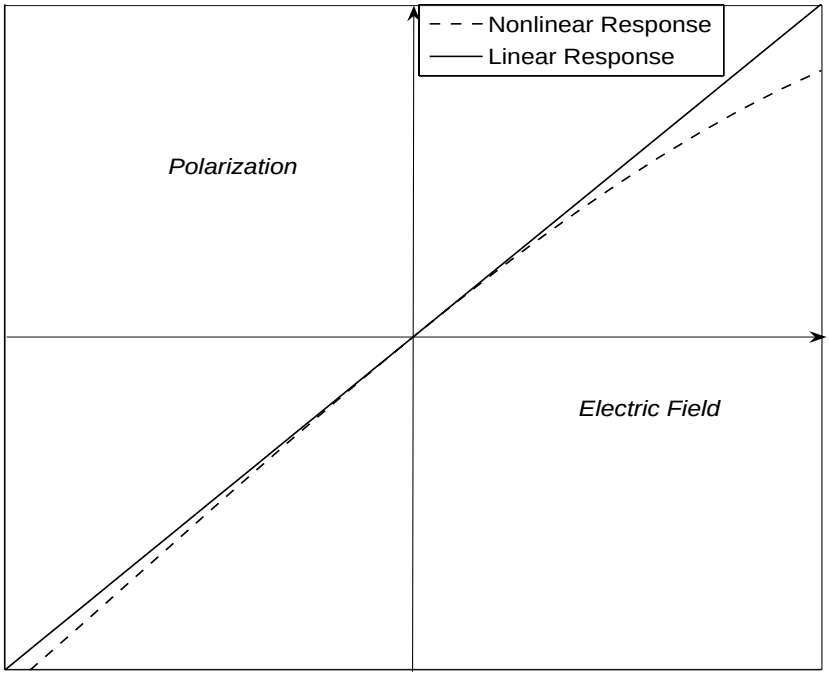

Figure 2.13. Linear response versus nonlinear response.

$$\begin{aligned} P_{\mathrm{NL}}^{(2)}(\mathbf{r},t) =& \frac{\epsilon_0\chi^{(2)}}{4}[\mathbf{E}_1^2 e^{2i\mathbf{k}_1\cdot\mathbf{r}}e^{-2i\omega_1 t} + 2\mathbf{E}_1\mathbf{E}_2 e^{-i(\omega_1+\omega_2)t}e^{i(\mathbf{k}_1+\mathbf{k}_2)\cdot\mathbf{r}} + \\ & \mathbf{E}_2^2 e^{-2i\omega_2 t}e^{2i\mathbf{k}_2\cdot\mathbf{r}} + 2\mathbf{E}_1\mathbf{E}_2^* e^{-i(\omega_1-\omega_2)t}e^{i(\mathbf{k}_1+\mathbf{k}_2)\cdot\mathbf{r}} + \mathrm{c.c.}] + \\ & \epsilon_0\chi^{(2)}\left[\mathbf{E}_1\mathbf{E}_1^* + \mathbf{E}_2\mathbf{E}_2^*\right]. \end{aligned} \tag{2.27}$$

Looking at the amplitudes of the different frequency components from equation (2.27) yields

$$\begin{aligned} P(2\omega_1) &= \frac{1}{4}\epsilon_0\chi^{(2)}E_1^2 \\ P(2\omega_2) &= \frac{1}{4}\epsilon_0\chi^{(2)}E_2^2 \\ P(\omega_1+\omega_2) &= \frac{1}{2}\epsilon_0\chi^{(2)}E_1E_2 \\ P(\omega_1-\omega_2) &= \frac{1}{2}\epsilon_0\chi^{(2)}E_1E_2^* \\ P(0) &= \frac{1}{4}\epsilon_0\chi^{(2)}\left(E_1E_1^* + E_2E_2^*\right). \end{aligned} \tag{2.28}$$

Second harmonic generation, or SHG, generates a second frequency at 2ω. *Sum frequency generation*, or SFG generates the sum of two incoming frequencies and

difference frequency generation, DFG consequently the difference. *Optical rectification* OR, is a special case when $\omega_1 = \omega_2$, and this produces a constant electric polarization in the medium.

Other effects can also be achieved from special cases of frequency mixing such as *parametric amplification* and *parametric oscillation* explained in section 2.6.

2.5.3 Nonlinear Susceptibility

The second order susceptibility tensor has 27 elements since explicitly written $\chi^{(2)} = \chi^{(2)}_{ijk}$, where the indices i, j, k are ranged over x, y and z and represents optical polarization direction. A convention in nonlinear optics uses the nonlinear d-matrix instead of the susceptibility tensor according to

$$d_{ijk} = \frac{1}{2}\chi^{(2)}_{ijk}. \tag{2.29}$$

Using the *Kleinman* symmetry [9] condition which states that the d-matrix is independent of frequency and independent of the permutation of indices $d_{ijk} = d_{ikj} = d_{jki}$ etc., the matrix can be contracted to a 3×6 matrix and we get [9]

$$\begin{pmatrix} P_x(\omega_3) \\ P_y(\omega_3) \\ P_z(\omega_3) \end{pmatrix} = 2\epsilon_0 \begin{pmatrix} d_{11} & d_{12} & d_{13} & d_{14} & d_{15} & d_{16} \\ d_{21} & d_{22} & d_{23} & d_{24} & d_{25} & d_{26} \\ d_{31} & d_{32} & d_{33} & d_{34} & d_{35} & d_{36} \end{pmatrix} \cdot \begin{pmatrix} E_x(\omega_1)E_x(\omega_2) \\ E_y(\omega_1)E_y(\omega_2) \\ E_z(\omega_1)E_z(\omega_2) \\ E_y(\omega_1)E_z(\omega_2) + E_y(\omega_1)E_z(\omega_2) \\ E_x(\omega_1)E_z(\omega_2) + E_x(\omega_1)E_z(\omega_2) \\ E_x(\omega_1)E_y(\omega_2) + E_x(\omega_1)E_y(\omega_2) \end{pmatrix} \tag{2.30}$$

The d-matrix is often replaced by an effective parameter d_{eff} that is calculated from the different nonlinear coefficients in the matrix and the optical polarizations involved. d_{eff} is in general a combination of one or more of the components d_{kl} in the contracted matrix. These components are then combined with trigonometric functions of the angles θ and ϕ, that describes the propagation direction of a wave in the crystal [6].

2.5.4 The Coupled Wave equations

From Maxwell's equations, it is possible to derive a set of coupled wave equations, which describes the interaction between the electromagnetic fields in the crystal. Taking into account the nonlinear terms, the wave equation can be written [6]

$$\nabla^2\mathbf{E} - \sigma\mu_0\frac{\partial\mathbf{E}}{\partial t} - \mu_0\epsilon\frac{\partial^2\mathbf{E}}{\partial t} = \mu_0\frac{\partial^2\mathbf{P}^{\mathrm{NL}}}{\partial t^2} \tag{2.31}$$

where σ is the conductivity, μ_0 the permeability and ϵ the dielectric constant. Assume a scalar field with its fourier components, propagating in the z-direction

at frequency ω_3

$$E(z,t) = \frac{1}{2}\left(E(z,\omega_3)e^{i(k_3 z-\omega_3 t)} + \text{c.c.}\right) \tag{2.32}$$

and a polarization at $\omega_3 = \omega_1 + \omega_2$

$$P^{\text{NL}}(z,t) = \frac{1}{2}\left(P^{\text{NL}}(z,\omega_1+\omega_2)e^{i((k_1+k_2)z-(\omega_1+\omega_2)t)} + \text{c.c.}\right) \tag{2.33}$$

with

$$P^{\text{NL}}(z,\omega_1+\omega_2) = 2\epsilon_0 d_{eff} E(z,\omega_1)E(z,\omega_2). \tag{2.34}$$

Equation (2.34) is given from the relation (2.30) using the effective nonlinear d_{eff} coefficient.

Three coupled wave equations can be derived with equations (2.32), (2.33) and (2.34) into the scalar version of (2.31) [6] resulting in

$$\begin{aligned}
\frac{d}{dz}A_1 &= -\frac{1}{2}\alpha_1 A_1 + i\gamma A_3 A_2^* e^{-i\Delta k z} \\
\frac{d}{dz}A_2 &= -\frac{1}{2}\alpha_2 A_2 + i\gamma A_3 A_1^* e^{-i\Delta k z} \\
\frac{d}{dz}A_3 &= -\frac{1}{2}\alpha_3 A_3 + i\gamma A_1 A_2 e^{i\Delta k z}
\end{aligned} \tag{2.35}$$

where

$$\begin{aligned}
A_i &= \left(\frac{n_i}{\omega_i}\right)^{1/2} E_i, \quad \text{for } i = 1,2,3 \\
\alpha_i &= \frac{\sigma_i}{n_i \epsilon_0 c}, \quad \text{for } i = 1,2,3 \\
\gamma &= \frac{d_{\text{eff}}}{c}\left(\frac{\omega_1\omega_2\omega_3}{n_1 n_2 n_3}\right)^{1/2} \\
\Delta k &= k_3 - k_2 - k_1, \text{ Momentum vectors for each wave.}
\end{aligned} \tag{2.36}$$

The wave vector $\mathbf{\Delta k}$, describes the relations between the wave vectors for the involving fields in equation (2.35). The relative phases of these fields are important in how the energy transfer between them occurs. The interaction works both ways so conversion can be done either from the driving pump field to the other two fields or the reverse.

2.6 Optical Parametric Oscillation

A special case of second order processes is optical parametric oscillation, or OPO. The induced nonlinear polarization in the crystal material couples the energy from the pump source into two new wavelengths, see equation (2.35). The pump photon is therefore split into two photons, called the signal and the idler. The main difference between the laser and the OPO, is that there are no atomic transitions in the crystal that generates the wavelengths. A doubly resonant cavity is illustrated in figure 2.14.

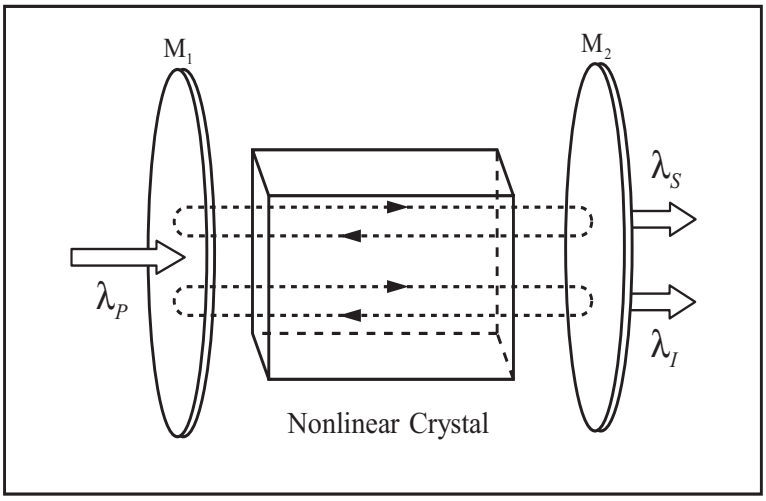

Figure 2.14. Doubly resonant optical parametric oscillator, meaning both signal and idler wavelengths are resonant.

The energy in the process must be conserved. For a given pump wavelength, there are many pairs of photons that satisfies the energy conservation. The specific pairs of photons generated is determined by the momentum or phase matching condition. These conversion processes can be summarized using the well known relations

$$\begin{aligned} \mathbf{E} &= \hbar\omega \\ \mathbf{p} &= \hbar\mathbf{k} \end{aligned} \tag{2.37}$$

to yield

$$\begin{aligned} \hbar\omega_p &= \hbar\omega_s + \hbar\omega_i, \text{ Energy conservation} \\ \hbar\mathbf{k}_p &= \hbar\mathbf{k}_s + \hbar\mathbf{k}_i, \text{ Momentum conservation} \end{aligned} \tag{2.38}$$

where the indices p, s and i denotes the *pump*, *signal* and *idler* fields respectively. By convention the frequency $\omega_s > \omega_i$. Due to the fact that energy can flow between the waves in three-wave mixing, described by equation (2.35), power is therefore transferred from the driving field at ω_p to ω_s and ω_i with gain for the frequency pairs that satisfies the momentum conservation.

Optical Parametric Oscillators have a wide range of tunability which is limited by the conservation of momentum, and the transparency range of the nonlinear crystal used. The choice of propagation direction in the crystal therefore allows the choice of tuning the signal and idler wavelengths. One can see this as having a control over the desired wavelength by the conservation requirement in equation (2.38). This wavelength selectivity feature is an advantage in for instance spectroscopy.

To obtain higher conversion efficiency, the crystal is placed in a separate cavity, either externally from the pump laser cavity or inside. When placed inside, the configuration can utilize the high internal intensity, which can be several orders of

magnitude higher than the out-coupled field. This configuration is referred to as an *Intracavity Optical Parametric Oscillator*. From the choice of mirrors this internal cavity can be made resonant for the signal wavelength called singly resonant SR, or double resonant DR for both signal and idler, or even triple resonant TR for all fields.

The OPO will function similar to a laser cavity, with a threshold to start the conversion and a round-trip gain in the KTP crystal. It can be shown [6] that the threshold intensity for the DR case is

$$I_{3th} = \left(\frac{n_3}{2Zd_{eff}^2}\right)\left[\frac{n_1 n_2 \lambda_1 \lambda_2}{(2\pi l)^2}\right](\gamma_1\gamma_2)$$

d_{eff} Effective nonlinear d-matrix coefficient

$Z = 1/\epsilon_0 c$ Free-space impedance (2.39)

$n_i,\ i = 1,2,3$ Refractive indices for signal, idler and pump.

$\gamma_j,\ j = 1,2$ Total loss per pass

λ_1, λ_2 Signal and idler wavelengths

The threshold for the singly resonant case is much higher than for the doubly resonant case. Doubly resonant OPO:s require simultaneous oscillations of both the signal and idler wavelengths. This requirement together with the requirement that conservation of the momentum and energy must be conserved, makes this setup more difficult to control [10].

2.7 Phase Matching

To obtain high conversion efficiency from the pump to the signal and idler, the fields needs to be phase matched. This can be achieved by the use of dispersive media, since a field will propagate with phase velocity according to

$$c_\omega = \frac{c}{n(\omega)} \tag{2.40}$$

where c is the speed of light in vacuum, and $n(\omega)$ the refractive index as a function of frequency.

For efficient energy flow we have already seen from equation (2.38) that the conservation of momentum requirement must be fulfilled. An alternative relation can be written using the refractive indices

$$\begin{aligned} n(\omega_p)\omega_p &= n(\omega_s)\omega_s + n(\omega_i)\omega_i \\ k_j &= \frac{2\pi\omega_j n(\omega_j)}{c}, \quad j = p, s, i. \end{aligned} \tag{2.41}$$

A technique to achieve the phase-matching condition is to use birefringent crystals. These crystals possess two indices of refraction that depends on the polarization and the direction of propagation [10]. The interacting waves with different frequencies are polarized differently, so by adjusting their phase velocities the requirement $\Delta\mathbf{k} = 0$ can be fulfilled.

The index of refraction is a function of wavelength and is described by the empirical Sellmeier equation [11]

$$n^2(\lambda) = A + \frac{B}{1 - \frac{C}{\lambda^2}} + \frac{D}{1 - \frac{E}{\lambda^2}} - F\lambda^2 \tag{2.42}$$

where the coefficients $A, B, \ldots, F$ are tabulated for different crystals. These equations have been presented in several different forms, where equation 2.42 with given coefficients, is a more refined version [11], giving small errors for wavelengths above 1μm. The coefficients often include a temperature dependence to describe temperature tuning of certain nonlinear crystals such as $LiNbO_3$. A plot of the Sellmeier equation can be seen in figure 2.15.

Figure 2.15. Plot of the refractive index as a function of wavelength for the nonlinear crystal KTP.

2.7.1 Uniaxial Crystals

The direction of symmetry in the crystal is called the optic axis (OA), and crystals with one OA are called *uniaxial*. Along this optical axis, both polarizations propagate with the same velocity. A wave that sees a constant index of refraction (ordinary index n_o) independent of its propagation direction is called an *ordinary wave*. The wave that sees an index dependent of propagation direction (extraordinary index $n_e(\theta)$) is called an *extraordinary wave*. The angle θ describes the direction of propagation relative the OA.

It is convenient to look at the cross section of the index surface for a uniaxial crystal, which can be described by the elliptic equation

$$\frac{x^2}{n_x^2} + \frac{z^2}{n_z^2} = 1. \tag{2.43}$$

where z is taken as the symmetry axis. If we let the coordinates x and z be expressed as a function of $n_e(\theta, \omega)$ we get

$$\begin{aligned} x &= n_e(\theta, \omega)\sin(\theta) \\ z &= n_e(\theta, \omega)\cos(\theta) \end{aligned} \tag{2.44}$$

and with equation (2.44) into equation (2.43) yields

$$\frac{1}{n_e^2(\theta, \omega)} = \frac{\sin^2(\theta)}{n_e^2(\omega)} + \frac{\cos^2(\theta)}{n_o^2(\omega)}. \tag{2.45}$$

With the use of equation (2.45) the phase matching angle can be calculated for both type-I and type-II phase matching for the desired frequency conversion process. Type-I phase matching is the situation when the signal and idler waves have the same polarization, while in Type-II their polarizations are orthogonal.

2.7.2 Biaxial Crystals

For biaxial crystals, such as KTP, two symmetry axes are present which by convention lie in the xz-plane, illustrated in figure 2.16. Since type-I phase matching for KTP have low nonlinear coefficients [10], type-II matching is most frequently used.

For a wave propagating along the optical axis, the refractive index is independent of polarization. For a wave propagating with wave vector $\mathbf{k}$, the indices of refraction are given by the Fresnel equation [3]

$$\frac{sin^2(\theta)cos^2(\varphi)}{n^{-2} - n_x^{-2}} + \frac{sin^2(\theta)sin^2(\varphi)}{n^{-2} - n_y^{-2}} + \frac{cos^2(\theta)}{n^{-2} - n_z^{-2}} = 0. \tag{2.46}$$

To calculate the phase matching angle for a biaxial crystal, the Fresnel equation (2.46) needs to be solved in conjunction with the Sellmeier equation and the type of phase matching condition considered. This is a quite complicated calculation, so the reader should refer to [12] or [13] for a detailed description. A calculated phase matching plot can be seen in figure 2.17, which displays the signal and idler wavelength as a function of the internal angle in the crystal.

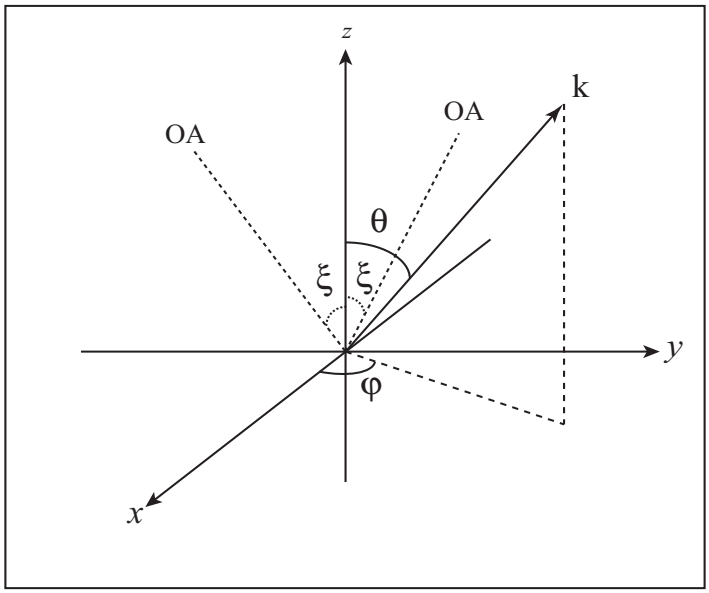

Figure 2.16. Coordinate system for a biaxial crystal with two optical axes OA.

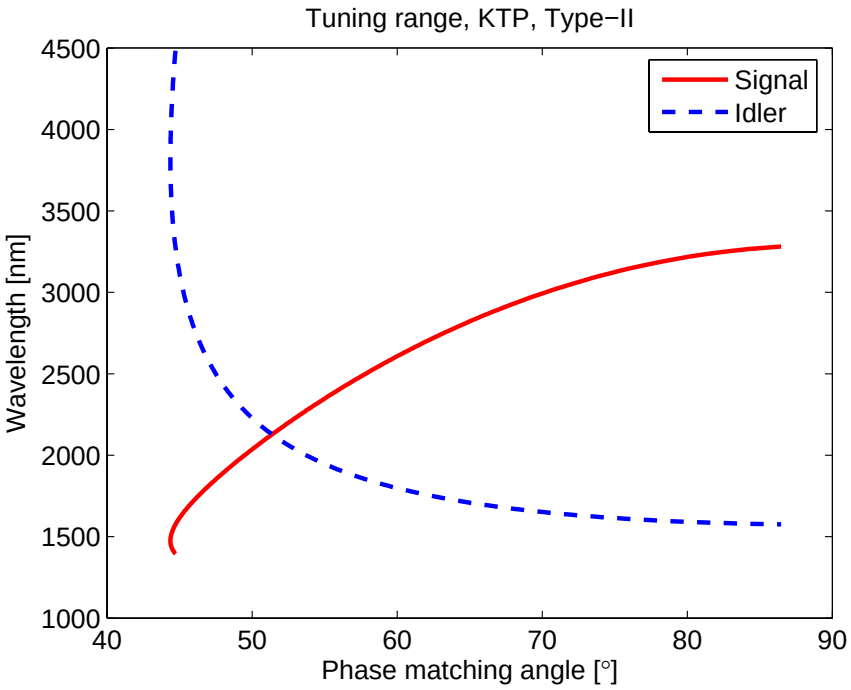

Figure 2.17. Calculated tuning range for Type-II KTP crystal pumped by 1064nm Nd:YAG at 300K. using the computer program SNLO [14].

Consider the type-II phase matching condition for an OPO

$$\mathbf{k}_{\mathrm{p}}(\mathrm{fast}) = \mathbf{k}_{\mathrm{s}}(\mathrm{fast}) + \mathbf{k}_{\mathrm{i}}(\mathrm{slow}) \tag{2.47}$$

where the designation *ordinary* and *extraordinary* for a uniaxial crystal is referred to as the *fast* and *slow* for a biaxial crystal [12]. A type-II matching for KTP indicates that the angle will be $\theta_m = 51.4°$ according to figure 2.17 giving a degenerate wavelength at $\lambda = 2128\,\text{nm}$.

2.7.3 Walk-off

In a birefringent crystal the propagation direction of the energy for the waves is in general not collinear. This means that the conversion efficiency will be limited.

The poynting vector is defined according to [15]

$$\begin{aligned} &\mathbf{S} = \epsilon_0 c^2 \mathbf{E} \times \mathbf{B} \\ &\mathbf{B}, \text{ Magnetic field} \end{aligned} \tag{2.48}$$

which is the power per unit area in the propagation direction. Now if critical phase

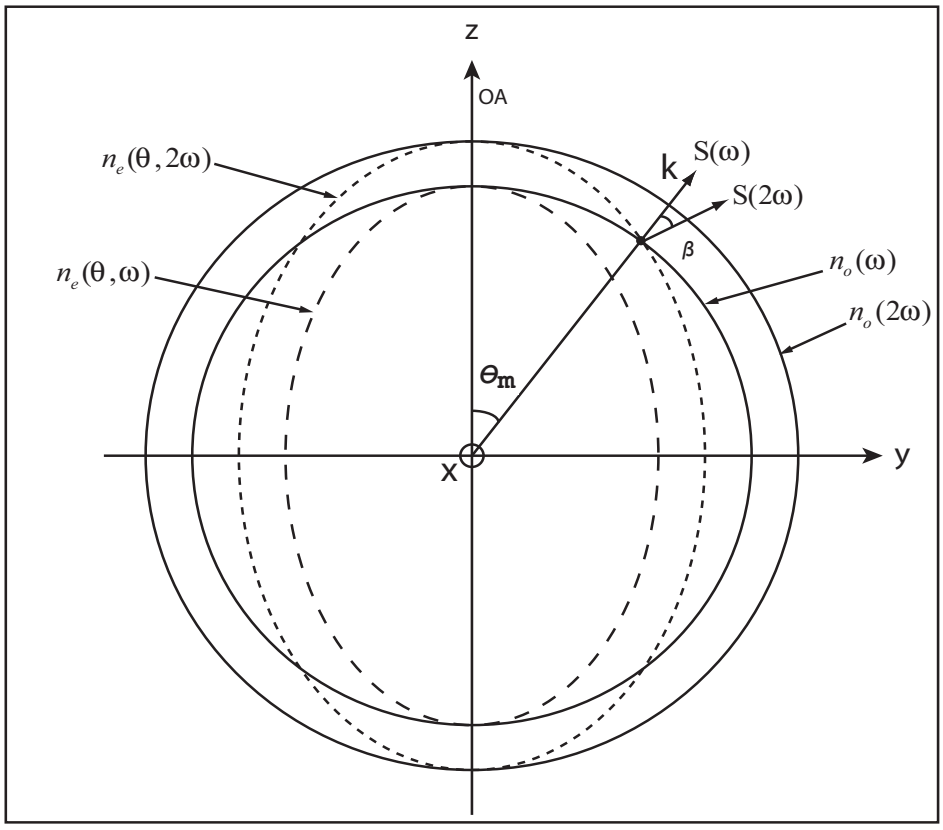

Figure 2.18. Second Harmonic (SHG) birefringent phase matching for a negative uniaxial crystal ($n_e < n_o$).

matched, the propagation direction between the fundamental and the harmonic will differ by an angle given by [11]

$$\tan(\beta) = \frac{n_o^2(\omega)}{2}\left(\frac{1}{n_e^2(2\omega)} - \frac{1}{n_o^2(2\omega)}\right) \tag{2.49}$$

for second harmonic generation, see section 2.5.2, as shown in figure 2.18. From figure 2.18 we see that no walk-off exists if $\theta_m = 90°$. When this condition is met, it maximizes the length of the nonlinear interaction that can be used. This is referred to as non-critical phase matching. Critical phase matching is done for all $\theta_m \neq 90°$. This means that walk-off effects now limits the conversion efficiency.

Chapter 3

Experimental Methods

3.1 Experimental Setup

A schematic drawing of the experimental setup is shown in figure 3.1. The plane-

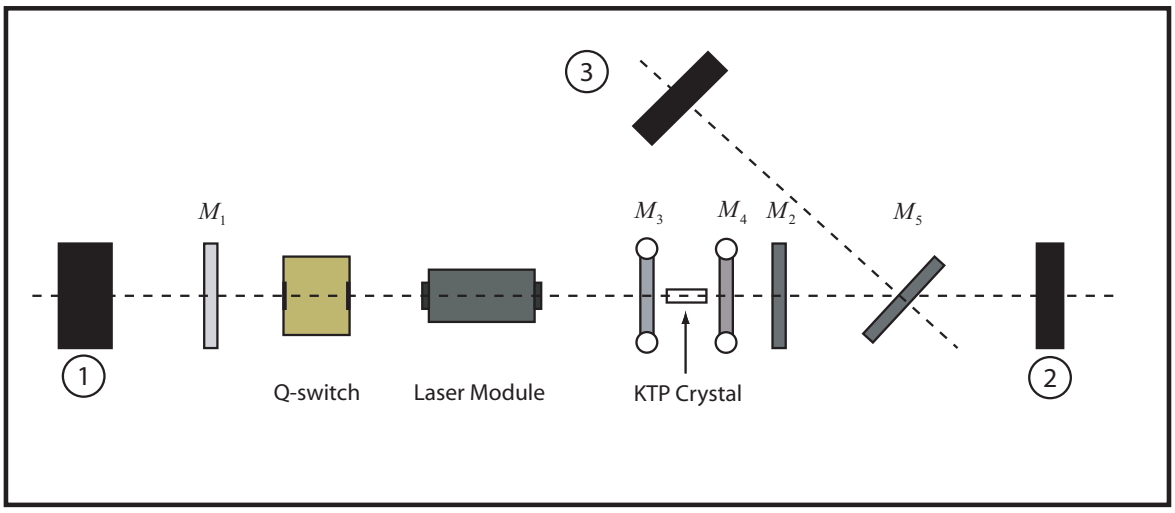

Figure 3.1. Schematic drawing of the experimental setup. Detectors for measurement of optical power are placed at positions 1, 2 and 3.

plane mirror pump-cavity uses a $M_1 = 75\%$ output coupling mirror at wavelength $\lambda = 1064\,\text{nm}$ and a highly reflecting mirror $M_2 \approx 100\%$. M_2 also has high transmittance in the $\lambda = 1.9 - 2.3\,\mu\text{m}$ region in order to couple out the signal and idler wavelengths.

The doubly resonant OPO cavity uses two mirrors, both with high transmittance at $\lambda = 1064\,\text{nm}$. M_3 is highly reflective in the $\lambda = 1.9 - 2.3\,\mu\text{m}$ region whereas M_4 is $70 - 80\%$ reflective in the same region. These mirrors are placed in dedicated holders with a two axis tip-tilt system to allow optimization of the internal cavity during lasing action.

To estimate the internal intensity in the cavity we have

$$P_{internal} = P_{out} \times \frac{1 + R_1}{1 - R_1} \tag{3.1}$$

where P_{out} is the measured output power at position 1 and R_1 the output mirror reflectance. An additional mirror M_5, with the same specifications as M_2, is used to filter out as much of the Nd:YAG wavelength as possible for more accurate readings of the converted radiation at position 2. Since mirror M_2 always transmits a small amount of Nd:YAG radiation due to the high internal cavity intensity, M_5 will reflect this part onto the detector at position 3 which together with the radiation at position 2 can be connected and simultaneously measured on a dual channel power meter. For a list of the used equipment see appendix C.

3.1.1 The Laser

The Nd:YAG laser rod used is side-pumped by diodes in arrays shown in figure 3.3. The pump wavelength from the diodes[1] is $\lambda_d = 808\,\text{nm}$ which produces the Nd:YAG wavelength at $\lambda = 1064\,\text{nm}$. The unit is also water cooled with a recirculating water cooler keeping the water at constant 22°C. This is important for the longevity of the diodes and to keep the thermal fluctuations to a minimum which results in a more stable laser output.

The pump module itself is compact with a Nd:YAG rod length of $l = 63\,\text{mm}$ and a diameter of $r_0 = 3\,\text{mm}$. The rod also has curved end faces ($\rho = -50\text{cm}$) to compensate the thermal lensing. For reasonable small cavity lengths powers up to 100 watts have been measured at position 1 with $M_1 = 75\%$ and $M_2 = 100\%$, both being plane. The maximum operating current for the pump module is 25 A. A picture of the fluorescence for the laser rod is shown in figure 3.2.

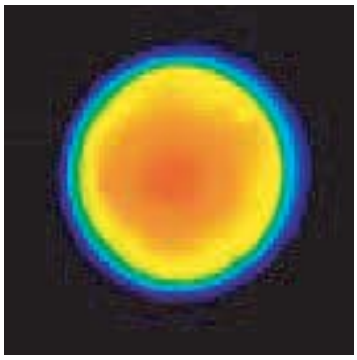

Figure 3.2. Flourescence for the Nd:YAG rod with radius 3 mm, 0.6% dopant. Picture taken from [17].

[1] The main advantage using diode pumping instead for instance arclamp pumping, is the fact that pumping close to the ideal absorption wavelength reduces the thermal absorption in the rod. Other advantages are higher efficiency compared to flashlamp pumping, higher beam quality and peak power and a smaller overall system [16].

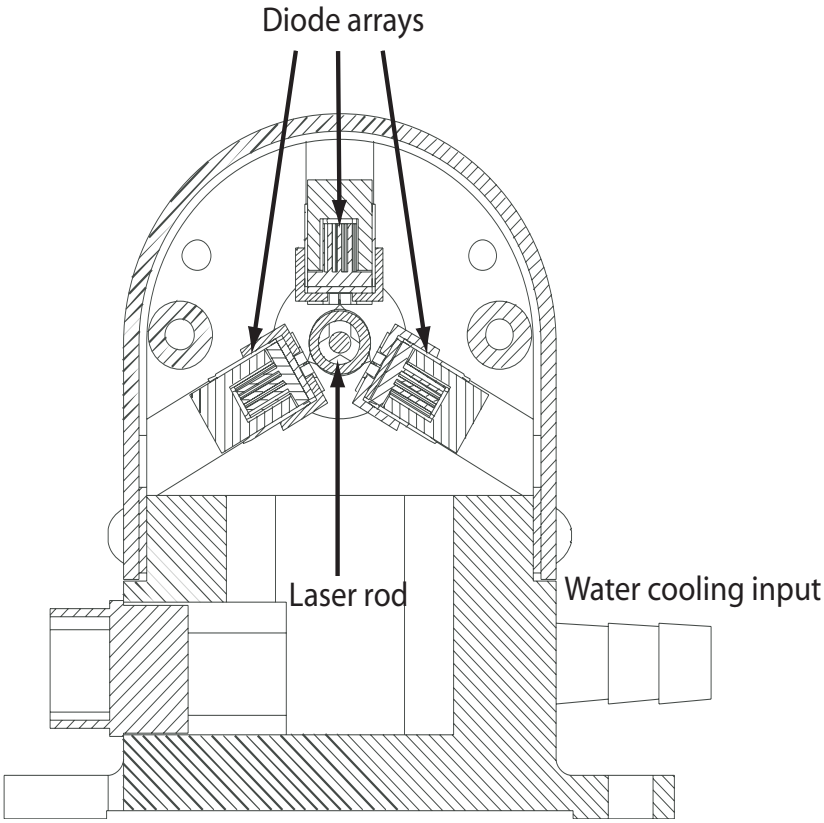

Figure 3.3. Cross section image of the CEO Laser module showing the diode arrays in a symmetric configuration for sidepumping the Nd:YAG rod. Picture taken from [17].

3.1.2 The KTP crystal

The nonlinear crystal is Potassium Titanyl Phosphate, $KTiOPO_4$ or KTP, a biaxial non-centrosymmetric crystal which has good properties for nonlinear optics such as large nonlinear coefficients and high damage threshold. KTP also has a broad transparency range as shown in figure 3.4. The crystal itself measures $5\times5\times15$mm and is cut 54° in the xz-plane to allow OPO degenerate wavelength conversion.

As with the laser rod, thermal effects are also present in the KTP crystal due to absorption of the interacting wavelengths. To keep the crystal at a constant temperature (and thermal gradients approximately radial), a cooling device was constructed shown in figure 3.5. The crystal is also antireflection coated for all involved wavelengths, in order to reduce the losses.

The crystal is placed in a holder made out of copper with good thermal conductivity. This copper holder is connected to a larger heat sink made of aluminium through two thermoelectric cooling elements. By applying a voltage to these elements, heat can be drawn from one side to the other. In order to compensate and keep the temperature constant a temperature controller regulates the applied voltage to these elements. A temperature sensor is placed in a drilled hole in the copper holder, close to the crystal and used as a reference temperature to the regulator.

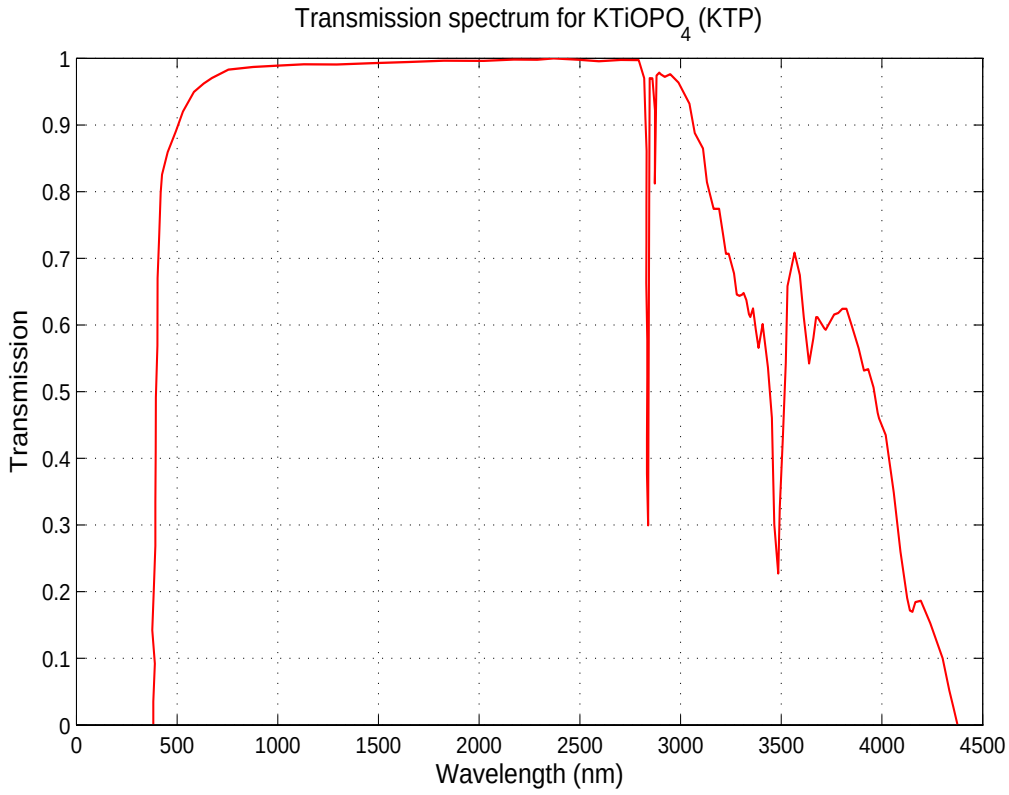

Figure 3.4. Transmission spectrum for Potassium Titanyl Phosphate [14].

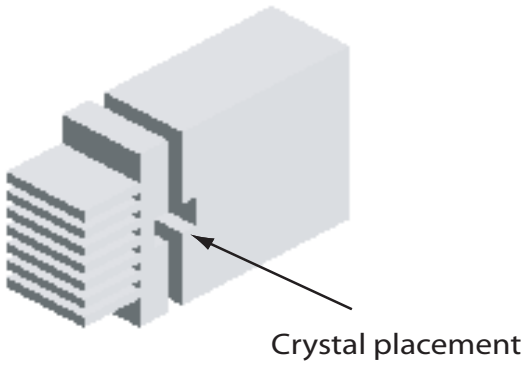

Figure 3.5. A perspective view of the copper cooling holder for the KTP crystal.

3.1.3 The Q-switch

The setup uses an acousto-optic Q-switch to pulse the Nd:YAG laser. Connected to a RF generator, a piezoelectric transducer converts electromagnetic energy into ultrasonic energy that travels through a transparent crystal which often is made of flint glass or fused Silica. This will in turn act as a phase grating diffracting a portion of the flux out of the cavity. The cavity losses increases and prevents oscillation. Turning the signal off again decreases the losses and a pulse is released. High repetition rate switching of the losses up to 50 kHz are possible using this model. A photo of the interior parts of the Q-switch is shown in figure 3.6.

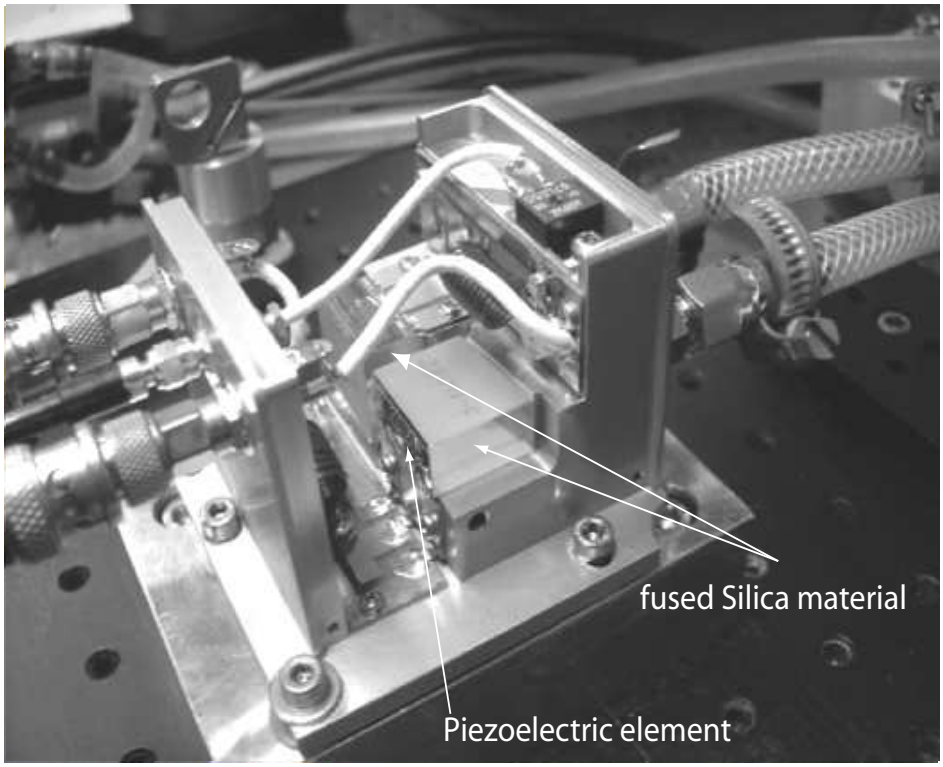

Figure 3.6. Image showing the piezoelectric transducer and the silica material acting as the phase grating.

3.2 Alignment of components

Before every measurement it is important to align all the optical elements in the system to ensure that maximum output power is obtained. This is accomplished using a HeNe laser as reference, placed to the right of position 1. Optimization is done by first aligning the components as good as possible with aid from the HeNe laser. At some fixed pump current above threshold, further optimization is done by adjusting the components so that the power output at position 1 is maximized. This procedure is first done for the plane-plane resonator by adjusting the mirrors M_1 and M_2 in figure 3.1. The procedure is then repeated introducing the Q-switch

in the cavity without pulsing the system, and again optimizing the same mirrors. Subsequently the same procedure is done with mirrors M_4 and M_3. In the last step the KTP crystal is placed between M_3 and M_4.

3.3 Methods for measuring the thermal lens

An important part of this work was to determine the focal length due to thermal lensing in the laser rod. This will provide information about the behavior of the rod which can be used in stability calculations of the cavity. These measurements were performed without the Q-switch and the internal cavity OPO of the resonator.

Two methods were used, one without laser oscillation of the Nd:YAG pump module, and one measurement with oscillation.

3.3.1 Method I

A simple experimental setup is shown in figure 3.7. Without laser oscillation of

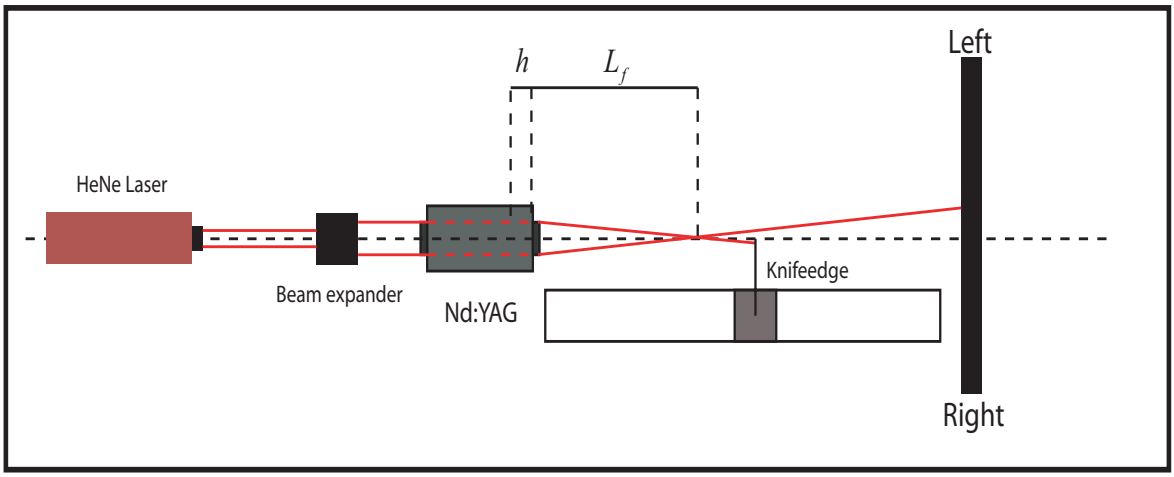

Figure 3.7. Measurement of refractive power with a HeNe laser as probe beam. A knife-edge is used to locate the focal spot.

the Nd:YAG, a HeNe laser[2] is used as a probe beam through the Nd:YAG laser. It is not necessary to use a probe beam that has the same emission spectrum that matches the spectrum of the Nd:YAG laser transition [5]. Using a HeNe laser in the visible region will essentially produce the same result. The beam will have a focus at a distance $L' = h + L_f$ measured from the principal plane of the laser rod. The distance to the focal point is for simplicity measured from the middle of the pump module and then recalculated to the principal planes of the laser rod. By varying the input pump current, the distance L' will be a function of the pump current. The beam expander is used to approximately collimate the HeNe laser before passing through the Nd:YAG rod. It also ensures that the HeNe laser probes the entire cross section of the laser rod.

[2] HeNe laser has a wavelength $\lambda = 633$ nm.

The distance is measured using a thin knife-edge that is slowly inserted in the path of the output HeNe beam from the Nd:YAG laser. The knife-edge is placed on a translation stage. By probing different distances noticing that when inserting the knife-edge behind the focal point the intensity distribution will start to decrease on the right side on the screen. Probing in front of the focal point will start to decrease the intensity pattern from the left instead. This method allows one to pinpoint the location of the focal length as a function of pump current. A drawback is that the method does not take the bifocusing into account from the thermal birefringence, described in section 2.4.

3.3.2 Method II

An alternative method is to determine the focal length when oscillation in the Nd:YAG laser is present. When oscillation takes place, a part of the input power is now converted to laser radiation which means that less heat is absorbed in the rod. The refractive power is therefore lower. This measurement should give a more accurate behavior of the refraction of the laser rod when the system is lasing. It will also take the bifocusing into account. An illustration of the setup is shown in figure 3.8. To perform the measurement, we now consider a symmetric setup with

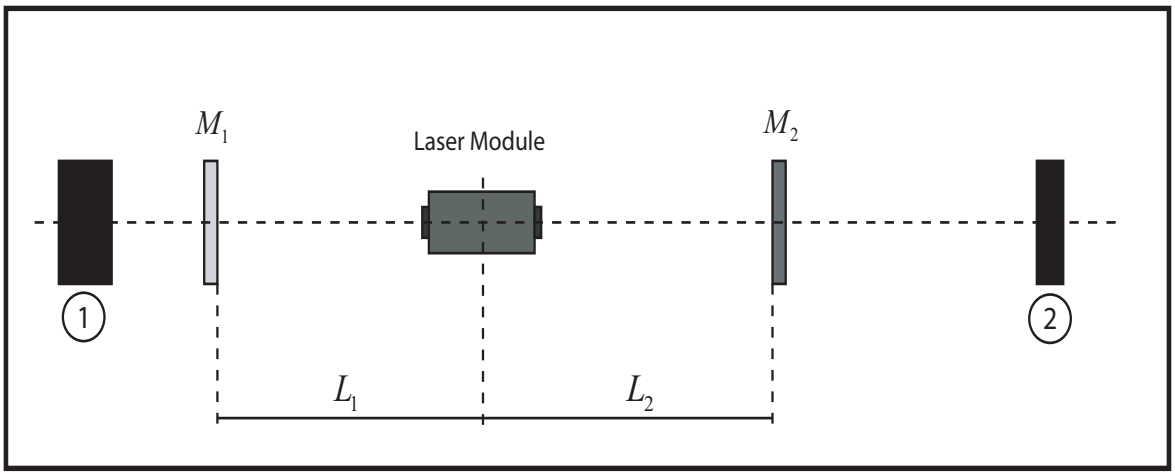

Figure 3.8. The setup used in Method II.

plane-plane mirrors of the resonator with the internal lens, see section 2.3.4. The stability diagram for this resonator is shown in figure 3.9.

For a symmetric resonator with plane-plane mirrors, this is represented by the straight line with three points A, B and C. Depending on input power, and therefore refractive strength of the rod, the equivalent resonator will change from plane parallel to confocal and finally concentric [18].

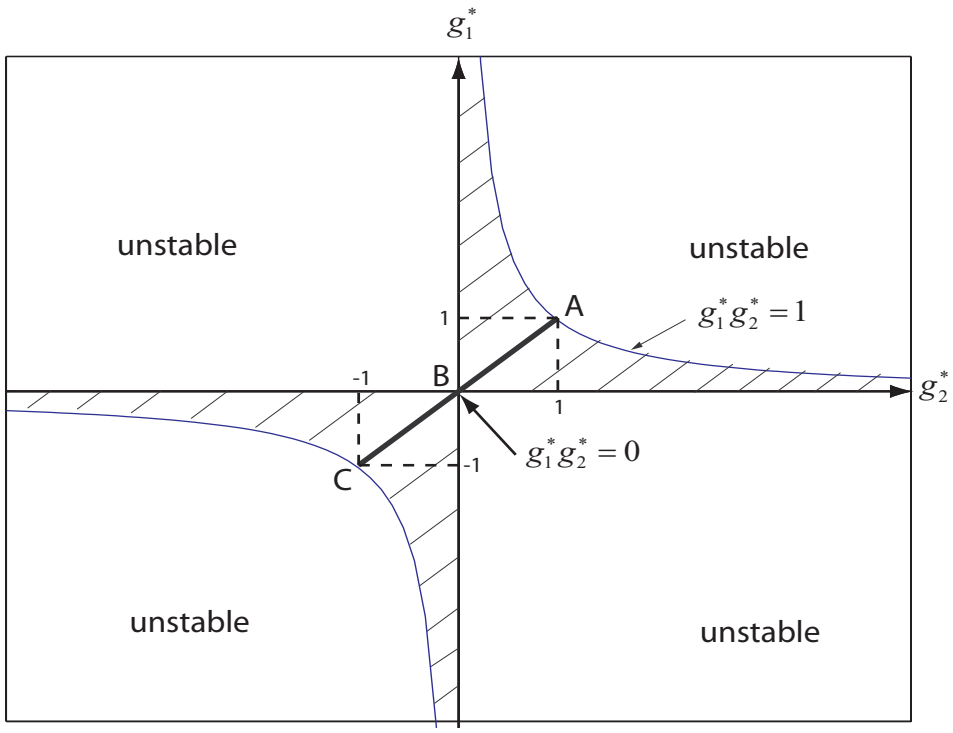

Figure 3.9. Stability diagram for a symmetric plane-plane resonator with an internal lens. Depending on input power the stability product $g_1^* g_2^*$ will move from point A to B and finally C.

From equation (2.15) we rewrite the relations

$$\begin{aligned} g_1^* &= 1 - Dd_2 - \frac{1}{\rho_1}\left(d_1 + d_2 - Dd_1 d_2\right) \\ g_2^* &= 1 - Dd_1 - \frac{1}{\rho_2}\left(d_1 + d_2 - Dd_1 d_2\right). \end{aligned} \tag{3.2}$$

The lengths to each mirror from the pump module are measured from the middle of the pump module, see figure 3.8. The total length is therefore $L = L_1 + L_2$. In the calculation of the refractive power D, the distances L_1 and L_2 must be recalculated to the principal planes of the rod, d_1 and d_2. The distance from the endfaces of the laser rod to the principal planes can be approximated by [19]

$$h = \frac{l}{2n_0} \tag{3.3}$$

where l is the laser rod length and n_0 the refractive index. For a plane-plane mirror cavity we have

$$\rho_1 = \rho_2 = \rho \approx \infty \Rightarrow \frac{1}{\rho} = 0. \tag{3.4}$$

Symmetric placement of the laser module means $L_1 = L_2$, and together with equations (3.2), (3.3) and (3.4) yields

$$\begin{aligned} g_i^* &= 1 - D \times \left[L_i - \frac{l}{2} \left(1 - \left(\frac{1}{n_0} \right) \right) \right] \\ L_i &= \frac{L}{2} \quad i = 1, 2. \end{aligned} \tag{3.5}$$

The stability of the resonator is therefore dependent on the length of the resonator and the refractive power of the internal lens.

Varying the pump current to the laser, means that the product $g_1^* g_2^*$ will travel on the straight line in figure 3.9. At the critical stable point **B** we have $g_1^* g_2^* = 0$ and the thermal lens is half of the resonator length. At this point there will be a decrease in measured output power. Since both a radial polarization and azimuthal polarization are present according to equation (2.18), the decrease will be a plateau region with the refractive power being higher for the radial polarization compared to the azimuthal.

By varying the length of the resonator, and performing measurements of the output power, the refractive powers can be determined at different pump powers. The power is measured at position 2 in figure 3.8, since the only detector able to cope with the high intensity at position 1, cannot collect data via interface to Labview. Despite the fact that mirror M_2 should have a theoretical reflectance of 100%, a fraction of the intensity will be transmitted, and this is instead used in the measurement at position 2.

In order to perform this measurement a Labview program was constructed. The program is able to control the laser driver current fed to the pump module in 0.1 A increments, which is the smallest increment possible. At each increment, the program measures the output power at position 2 in figure 3.8.

Since the output power were noticed to fluctuate due to thermal issues, the program takes the average from 15 values collected on the power meter connected to the detector placed at position 2. The time between these measured values is $t_{meas} = 0.5$ s. The program also executes a warmup stage in order to reach a working temperature for the system. This is done by increasing the pump current to the maximum value $I_p = 25$ A and wait for approximately 60 s. The current is then decreased to the start value, and again waiting approximately 30 s. Between each increase of the pump current, the system is delayed 10 s, in order to stabilize the system at each new pump current fed to the laser module. The program also acquires the diode array and laser driver temperature.

Performing this measurement for different lengths of the symmetric cavity will provide information about the focal length from the plateau regions that occur. The measurement will also provide an estimate of the efficiency factor η in equation (2.18) that gives information about the amount of heat generated in the laser rod when lasing occurs.

3.4 Optical Parametric Measurements

By pulsing the Nd:YAG laser, the threshold for conversion in the KTP crystal is reached more easily than for continuous wave operation. The converted radiation from the OPO is measured at position 2, see figure 3.1. Two photodiodes with fast rise times are placed to measure the output pulses both from the Nd:YAG and the OPO. Since both diodes are too sensitive for direct radiation measurement, they are placed near each detector placed at position 1 and 2 to measure the diffuse reflection of the radiation. From these photodiodes the pulse stability and pulse length from the Nd:YAG and the OPO have been analyzed with an oscilloscope.

A number of different cavity lengths were tested. Both symmetric setups, where the laser module was placed in the middle of the cavity, and nonsymmetric setups have been analyzed. In order to be able to fit the internal cavity parts, the nonsymmetric setups consisted of moving the laser module and Q-switch closer to the output coupling mirror M_1. Another reason was to prevent damage to the Nd:YAG rod, since placing the pump module too close to the internal cavity can produce a focus on the laser rod. This is possible since the waist produced at M_2 can be partly reflected by M_3 and cause damage.

By using a grating monochromator, the spectra of the signal and idler wavelengths were measured and verified with the energy conservation relation

$$\frac{1}{\lambda_p} = \frac{1}{\lambda_s} + \frac{1}{\lambda_i}. \tag{3.6}$$

If the crystal is rotated slightly in the OPO cavity, it will be possible to tune different wavelengths satisfying the momentum conservation (2.38). The fulfilled wavelengths can again be seen from figure 2.17 in section 2.7.

Chapter 4

Results

4.1 Thermal Lensing

4.1.1 Method I Results

The result of the focal length measurement is presented in figure 4.1.

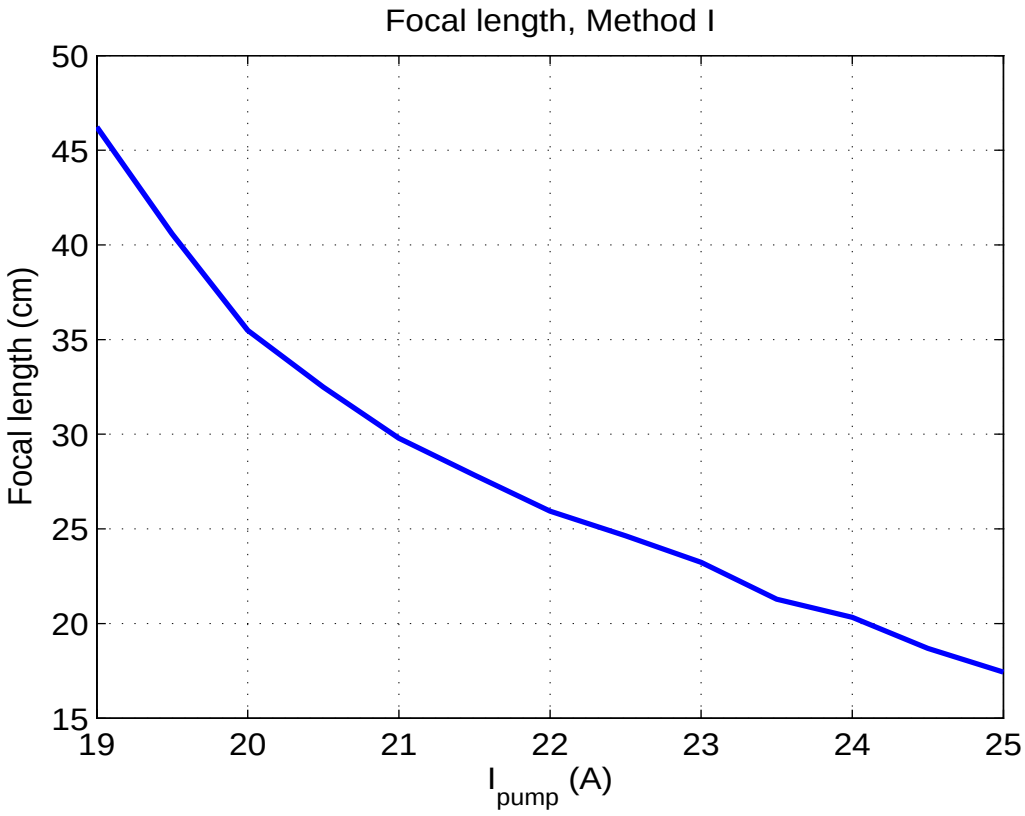

Figure 4.1. Measurement of the focal length as a function of pump current, using method I.

To verify that the refractive power followed a linear dependence according to equation (2.18), $D = 1/f$ is therefore plotted in figure 4.2. In contracted notation (2.18) can be written

$$D = \sigma_{r,\phi} P_a + \kappa \tag{4.1}$$

with

$$\begin{aligned} \sigma_{r,\phi} &= \frac{1}{KA}\left(\frac{1}{2}\frac{dn}{dT} + \alpha C_{r,\phi} n_0^3 + \frac{\alpha r_0 (n_0 - 1)}{L}\right) \\ P_a &= \eta V \times (I_p - I_{th}) \\ \kappa &= -\frac{2(n_0 - 1)}{\rho_0} \end{aligned} \tag{4.2}$$

It is important to remember that (4.1) contains both a radial and azimuthal dependent focal length. The performed measurement did not take this into account, so figure 4.1 shows the effective focal length.

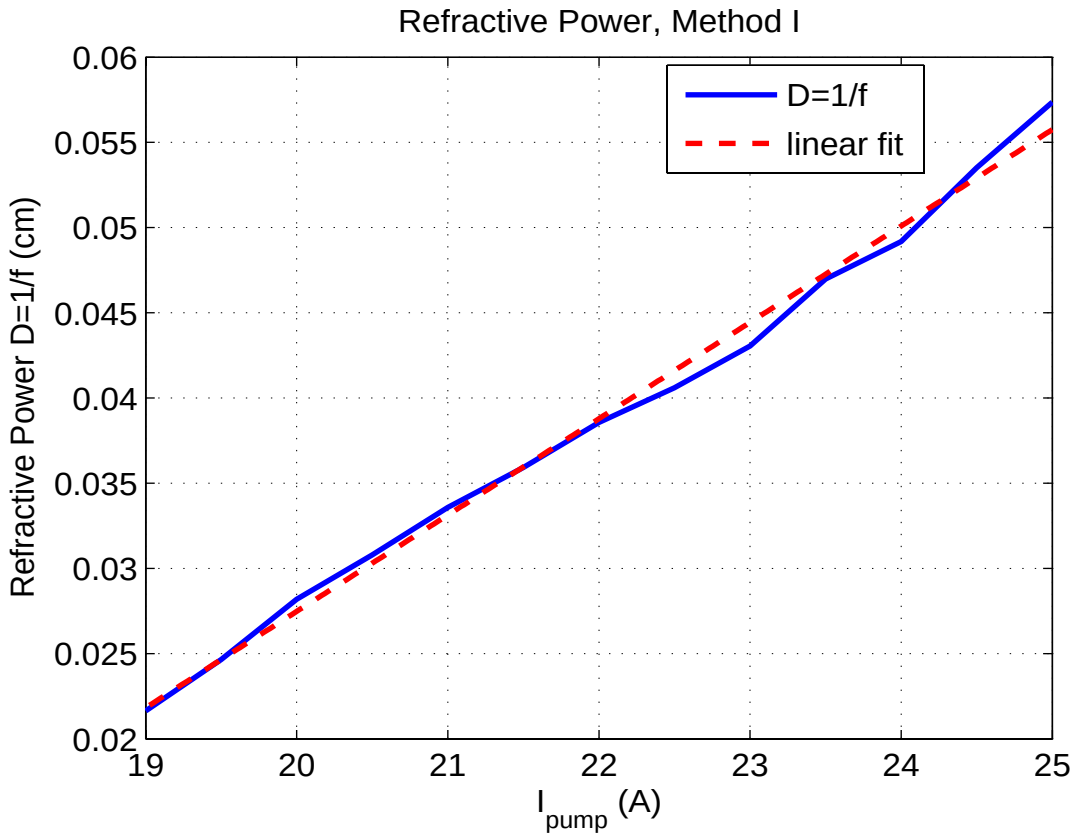

Figure 4.2. Plot showing the refractive power $D = 1/f$ together with a linear fit as a function of pump current.

From equation (4.1) the only term contributing to the refraction up to the point when $I_p = I_{th}$, is κ. Taking the linear fit curve of the refractive power, and plotting this with κ, the intersection should give an approximate estimation of the diode

threshold current, see figure 4.3. The calculation is done numerically based on the linear fit data.

From the linear fit equation together with the constant κ we get

$$I_{th} \approx 9.4 \text{ A}$$

which is a reasonable result for the diode arrays. Estimating the overall efficiency

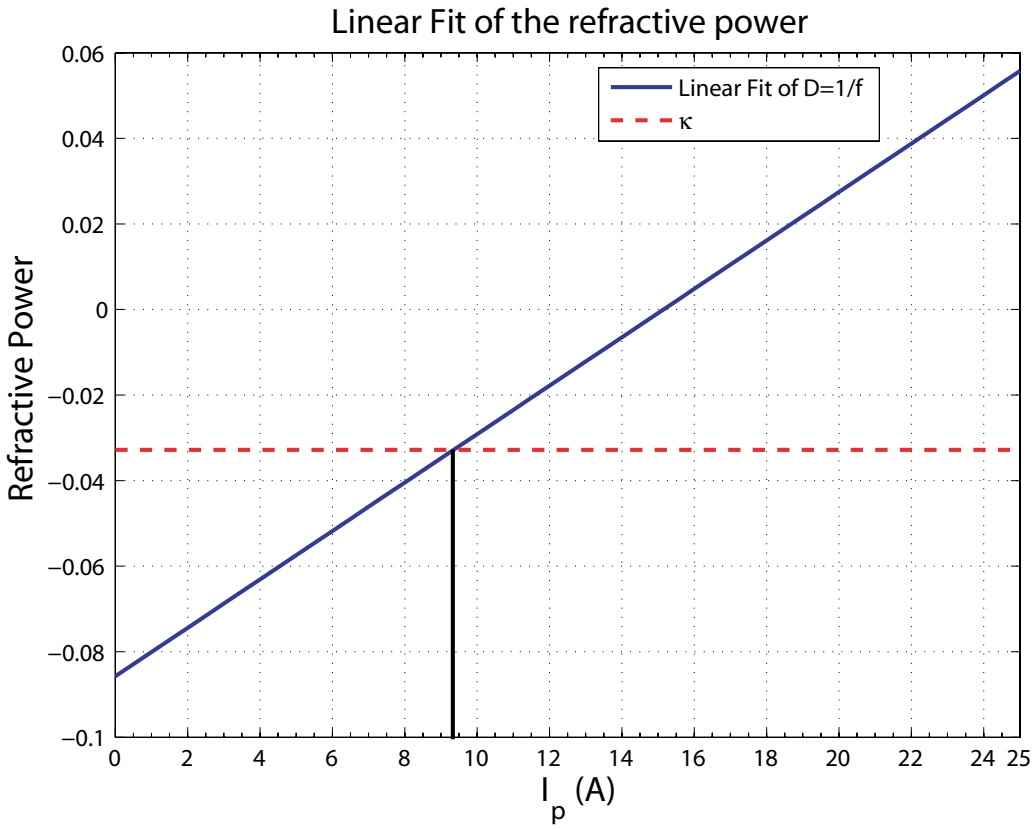

Figure 4.3. Plot showing the refractive power $D = 1/f$ together with the constant κ. At the intersection, the value of I_{th} can be calculated.

η can be done from equation (4.1) with equation (2.19)

$$D = \sigma_{av} P_a + \kappa = \sigma_{av} \eta V \left(I_p - I_{th}\right) - \frac{2(n_0 - 1)}{\rho_0} \tag{4.3}$$

where

$$\sigma_{av} = \frac{\sigma_r + \sigma_\phi}{2} \tag{4.4}$$

if it is assumed that the measurement gives the mean focal length. Again using the least-square method for the fit, η can be calculated from

$$\eta = \frac{D - \frac{2(n_0 - 1)}{\rho_0}}{\sigma_{av} \cdot V \left(I_p - I_{th}\right)}. \tag{4.5}$$

The method gives $\eta \approx 40\%$. To verify that this value is reasonable, the separate terms in η needs to be analyzed. From [3]

$$\begin{aligned} P_a &= \eta P_{in} \\ \eta &= \eta_p \eta_T \eta_a \eta_f \\ \eta_d &= \text{ Diode Efficiency} \\ \eta_T &= \text{Transfer Efficiency} \\ \eta_a &= \text{ Absorption Efficiency} \\ \eta_f &= \text{ Fluorescence Efficiency} \end{aligned} \tag{4.6}$$

where

$$P_{in} = V\left(I_p - I_{th}\right). \tag{4.7}$$

is the electrical input power from the laser driver. The effective efficiency factor is a rather complex parameter, since it depends on several other efficiency parameters. The *diode efficiency* factor determines how efficiently the pump diodes will convert the electrical power input to actual optical pump radiation. The *transfer efficiency* describes the amount of useful pump radiation from the pump source to the gain medium. The *absorption efficiency* factor determines how much that is actually absorbed from the pump radiation in the Nd:YAG rod. The *fluorescence efficiency* determines how much of the absorbed pump power that is converted to heat in the rod without lasing action.

From [3] these parameters can be approximated

$$\begin{aligned} \eta_d &\approx 0.5 \\ \eta_T &\approx 0.95 \\ \eta_a &\approx 0.9 \\ \eta_f &\approx 0.43 \end{aligned} \tag{4.8}$$

and this gives $\eta \approx 19\%$, a difference by a factor 2. The result for the measured η should be taken as an estimate of the real value. This large difference could mean that more heat was absorbed in the rod than estimated from the values used in (4.8). It could also be from the uncertainty in the data collected during the measurement.

There are a couple of reasons explaining the result.

1. We are dealing with two focal points, created from the two different polarizations due to birefringence effects in the rod. The method did not take this into account.

2. This method can be cumbersome, since it was hard to observe how the intensity pattern on the screen changed when probing with the knife edge.

3. The values for all the involved efficiency parameters are typical values obtained from [3], and will not perfectly describe this particular system.

With these facts in mind it can be concluded that Method I gives an approximate description of the behavior of the refractive power of the laser rod.

4.1.2 Method II Results

Four different symmetric cavity setups were measured with this method. The mirrors were plane-plane, with the output coupling mirror $M_1 = 75\%$. The different cavity lengths were $L = 40, 60, 80, 100$ cm. The initial value of the diode current was $I_{start} = 18$ A.

From the images in figure 4.4, a number of observations can be made. Firstly the stability of the resonator for high pump currents clearly decreases with the length of the resonator. This is to be expected, since the refractive power of the rod is large enough to make the resonator unstable. For $L = 100$ cm a sudden drop in output power at $I_p \approx 24.5$ A can be seen. This is since the stability criterion for the g-parameters is no longer fulfilled, see section 2.3.4, and the rays are no longer confined within the cavity. The output power therefore decreases rapidly.

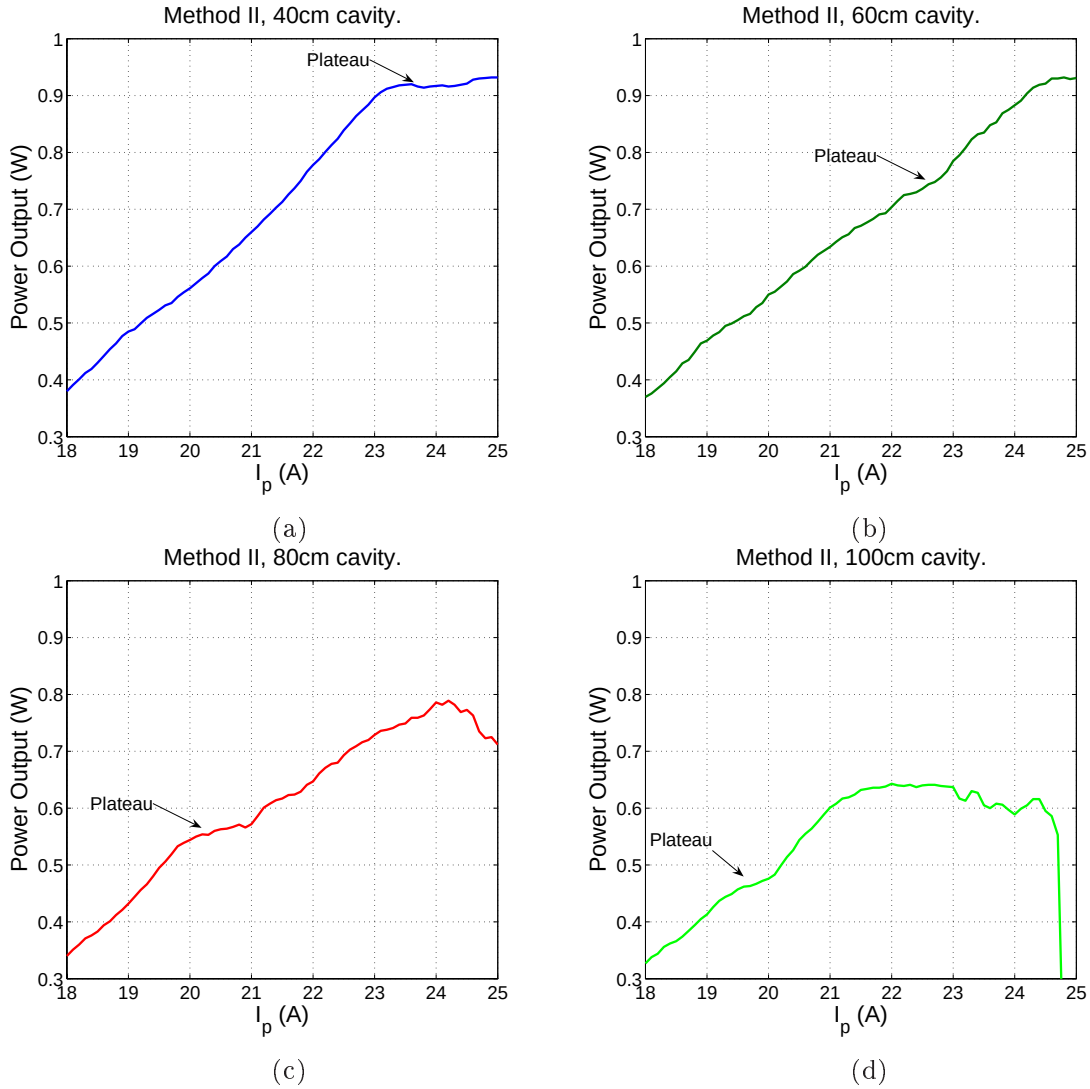

Figure 4.4. Measurement of the output power, using Method II. a) 40 cm, b) 60 cm, c) 80 cm and d) 100 cm.

The graphs in figure 4.4 exhibits a fairly linear relation between P_{out} and I_p until a

plateau region appears. The plateau regions in figure 4.4 are established when the output power does not increase linearly as input power increases. This decrease means that the resonator has reached the point **B** in figure 3.9. From equation (4.1) and (4.2), the refractive power of the radially polarized light is higher compared to the refractive power of the azimuthal polarization. This is true since the photoelastic coefficient for Nd:YAG have different values ($C_r = 0.0017, C_\phi = -0.0025$) for the radial and azimuthal polarizations according to [3]. The first knee-point in figure 4.4 therefore corresponds to D_r and the second knee-point to D_ϕ. Between these two points the effective refractive power is obtained.

From figure 4.4, it can be difficult to locate these plateau regions with high accuracy. For the 60 cm case, the plateau region is hard to spot. From theory, the plateau region will move down in the graph as the length of the resonator increase. A faint decrease for the 60 cm case can be located at the marked spot in figure 4.4.

Since the focal lengths f_ϕ and f_r are exactly half the length of the cavity at the plateau regions, it is possible to plot the refractive powers from the collected points and use a linear fit. For the 40 cm cavity, the knee-point for D_ϕ is hard to determine since the maximum pump current for the system is $I_p = 25$ A. The number of measured points for D_ϕ in the linear fit will therefore be restricted to three. For D_r, four points can be used in the fit.

From equation (4.1), the located points for both refractive powers are plotted together with the corresponding linear fits. The result is presented in figure 4.5. The calculated values for the efficiency parameter will be $\eta \approx 37\%$ using the D_ϕ

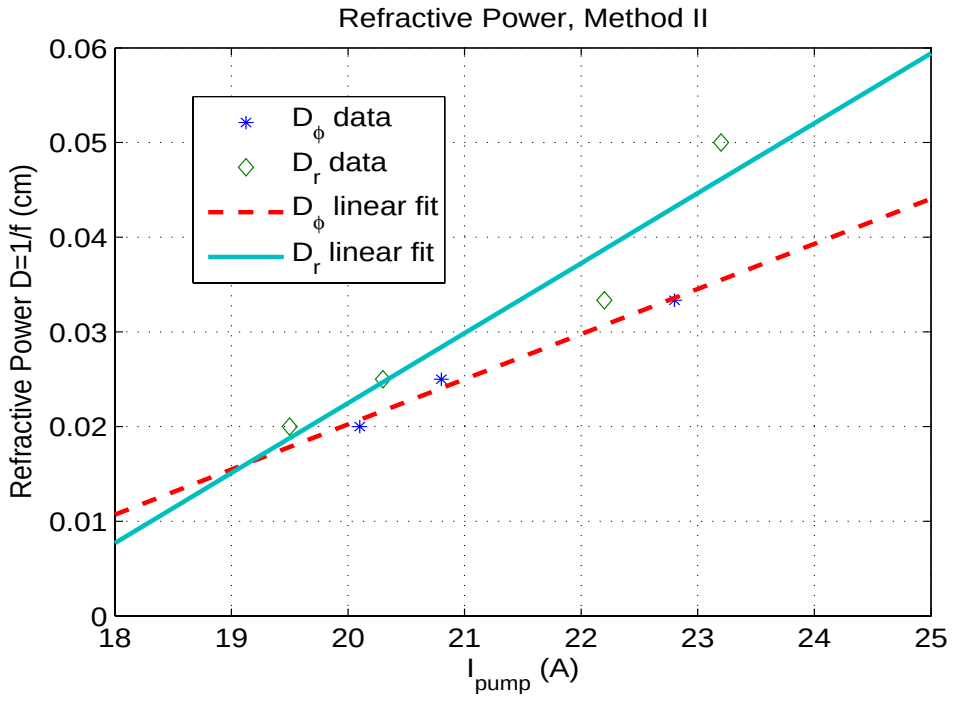

Figure 4.5. Refractive power measurement, using Method II. The data points for both D_ϕ and D_r are shown, together with a linear fit using least square fit method.

data, and $\eta \approx 47\%$ for D_r. This result suggests two different efficiency factors. The factor should be the same for both the measurements according to equation (4.1) and the slope of the two plots in figure 4.5 should be the same.

Since there is an uncertainty determining where the actual plateau regions are in figure 4.4, the calculations are probable to show a difference in calculated values for the refractive powers. To verify that the parameter is within a reasonable interval, the parameters in equation (4.8) are again used with a slight modification. The parameter for the fluorescence will now be replaced with η_t which determines how much of the absorbed pump power that is converted to heat in the rod with lasing action. A typical value for this parameter $\eta_t \approx 32\%$ [3] and this results in a total efficiency $\eta \approx 14\%$.

In Method I the threshold current for the diodes was estimated. This can also be done in Method II. The result is presented in figure 4.6.

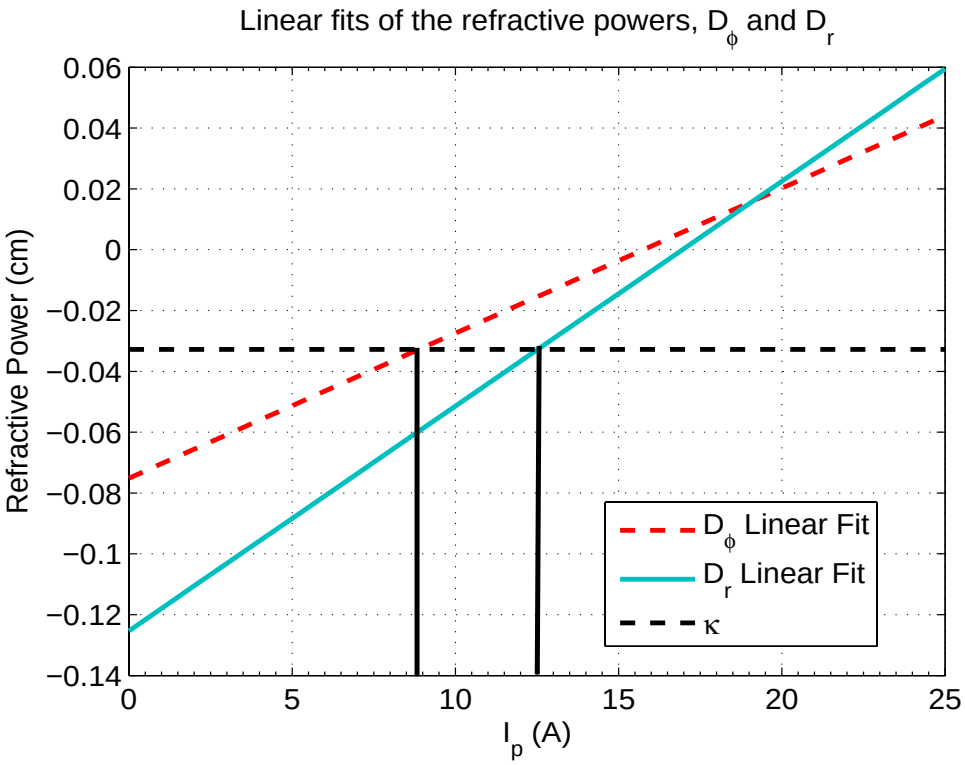

Figure 4.6. Plot showing the refractive powers D_ϕ and D_r together with the constant κ. At the intersections, the value of I_{th} can be estimated.

From picture 4.6, two different values of the threshold current are obtained. At the intersection the linear fit of D_ϕ give $I_{th} \approx 8.8$ A, and using D_r we get the value $I_{th} \approx 12.5$ A. Comparing these values, it seems that the most reasonable value for the threshold current is 8.8 A, using the linear fit for D_ϕ. If these values are compared to the value obtained in Method I, the difference in result is approximately 6.4% using the D_ϕ fit compared to 33% using the D_r fit.

From theory we know that η is lower when lasing takes place. This is true since the laser is now converting part of the electrical input power to laser radiation. The

calculated value in Method II should therefore be lower than the value obtained in Method I. From Method II, $\eta \approx 37\%$ seems to provide the most reasonable value. The difference between the estimated values and measured values for η are still large in both methods. This can either be related to the high uncertainty in the measured values, or that more heat actually is absorbed in the laser rod.

Method II assumes that the measured power doesn't drop before the unstable region **B** is reached. If the power dropped earlier before the point, it could be one explanation for the difference in results for η. The result suggests that there are a number of instability issues in the system, affecting the measurements. If output power from the laser system fluctuates it will in turn affect the result. An analysis of the thermal issues and output power stability is required.

4.2 Power Stability

During lasing action, there will be thermal effects in the components in the system. The Nd:YAG rod will act as a thick lens with a refractive power depending on the pump current. Additionally there will be thermal effects in the mirrors. It is of interest to measure the output power from the system in order to explore the thermal effects. By using a modified version of the Labview program, the output power was measured continuously during a time-period. The experimental setup is shown in figure 4.7. By using a beam-sampler, a fraction of the intense output radiation at the output coupling mirror M_1 could be simultaneously measured together with the output power at mirror M_2. The Labview program increases the

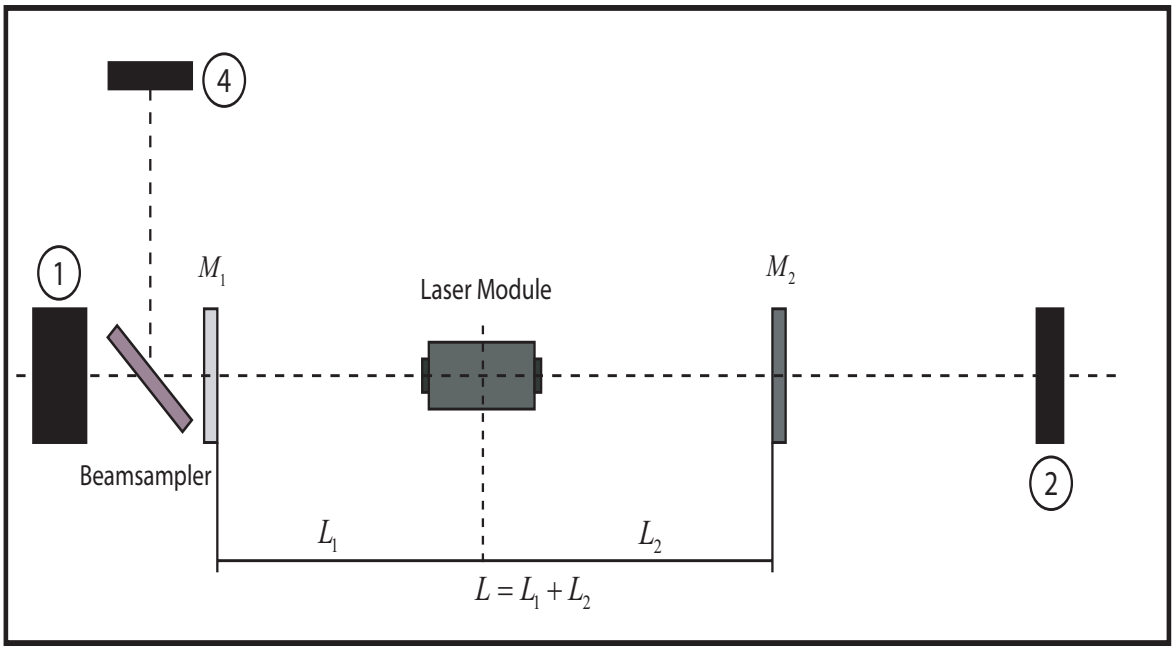

Figure 4.7. Power measurement setup, using a beam-sampler. The cavity length was $L = 60$ cm. The detectors used, see appendix C, was 1) Ophir-10000 W, 2) PM3 and 4) PM10.

pump current to a chosen fix value. The power at both detectors recorded values for a chosen period of time. The cavity used was $L = 60\,\text{cm}$ and symmetric. The result can be seen in figure 4.8. At position 4 the time evolution of the output

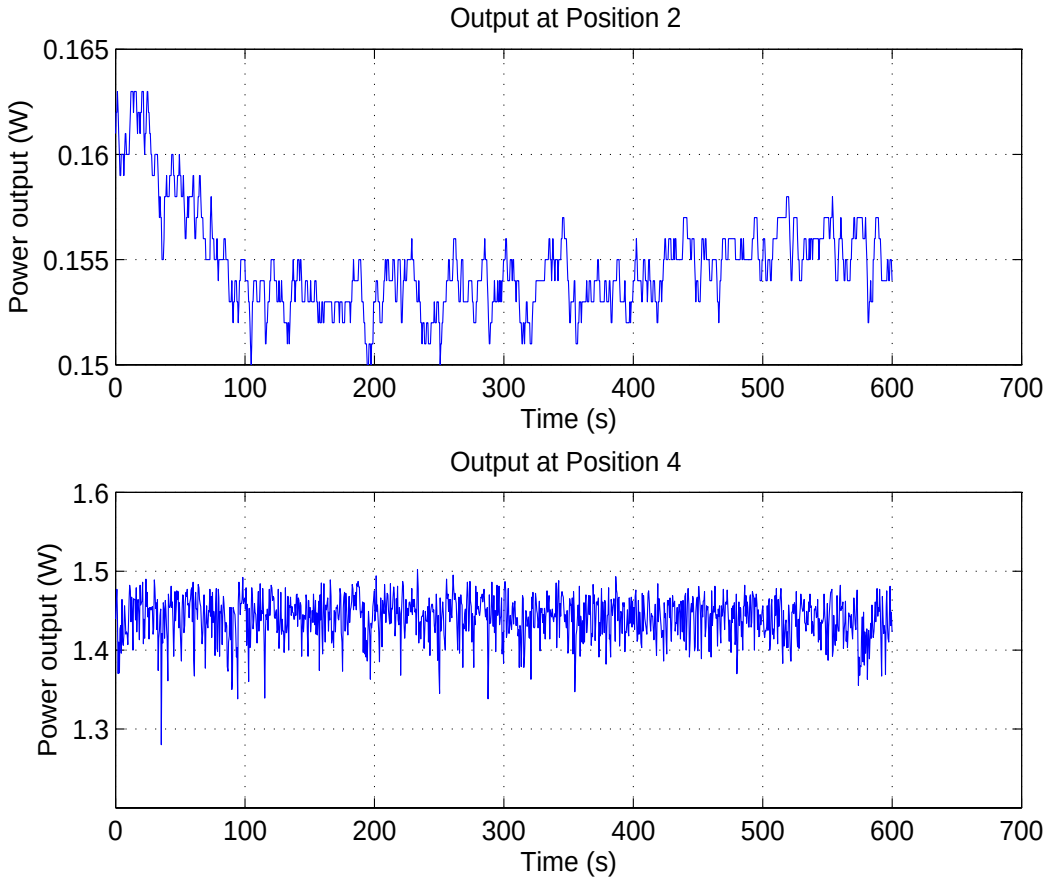

Figure 4.8. Measured output power at position 4 and position 2. The pump current is fixed at $I_p = 18\,\text{A}$ and total time is $t = 10\,\text{min}$.

power was roughly constant. This was not the case for the power measured at position 2. There seems to be an oscillation in the output power until it settles after roughly 6 minutes. Since the two detectors used are not the same model, the measurement was performed again by switching the position for the detectors[1]. The result is presented in figure 4.9.

From figures 4.8 and 4.9 it can be concluded that the change in output power is reproducible and independent of detector used. This suggests that there is a thermal instability producing the fluctuations seen at mirror 2. From figure 4.9 we see that these fluctuations settle after $t \approx 300\,\text{s}$. The output power from mirror 1 follows a fairly similar time evolution as in figure 4.8. For $t > 300\,\text{s}$ the variation in power is less than 11% at mirror 2, and less than 4% at mirror 1. The results

[1] The laser is shut down for a brief period of time in order to switch the detectors. This is also necessary in order to reproduce the same measurement.

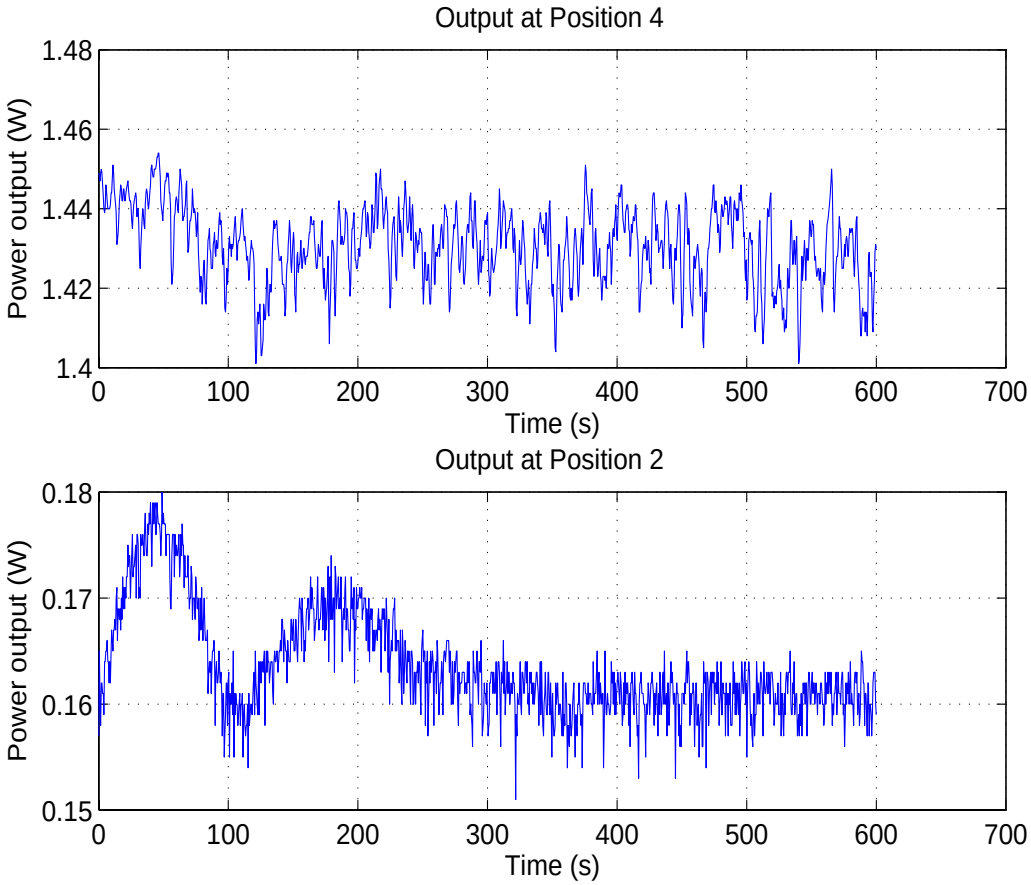

Figure 4.9. Measured output power switching the detectors. The pump current is fixed at $I_p = 18$ A and total time is $t = 10$ min.

therefore suggest that there is a small absorption of power in the mirrors which affect the output power.

In order to see how the fluctuation depends on the pump current used, a final measurement was done starting off by waiting approximately 300 s at $I_p = 18$ A, and then increasing the pump current to $I_p = 20$ A. The result is presented in figure 4.10 and again indicates that the time until the system reaches a working temperature is approximately $t \approx 300$ s.

During these measurements the diode array temperature in the laser module was also collected, see figure 4.11. It is important that this temperature for the arrays does not fluctuate, since this would mean that the radiation from the pump module itself could account for the power fluctuations. The array temperature was more or less constant, which was expected.

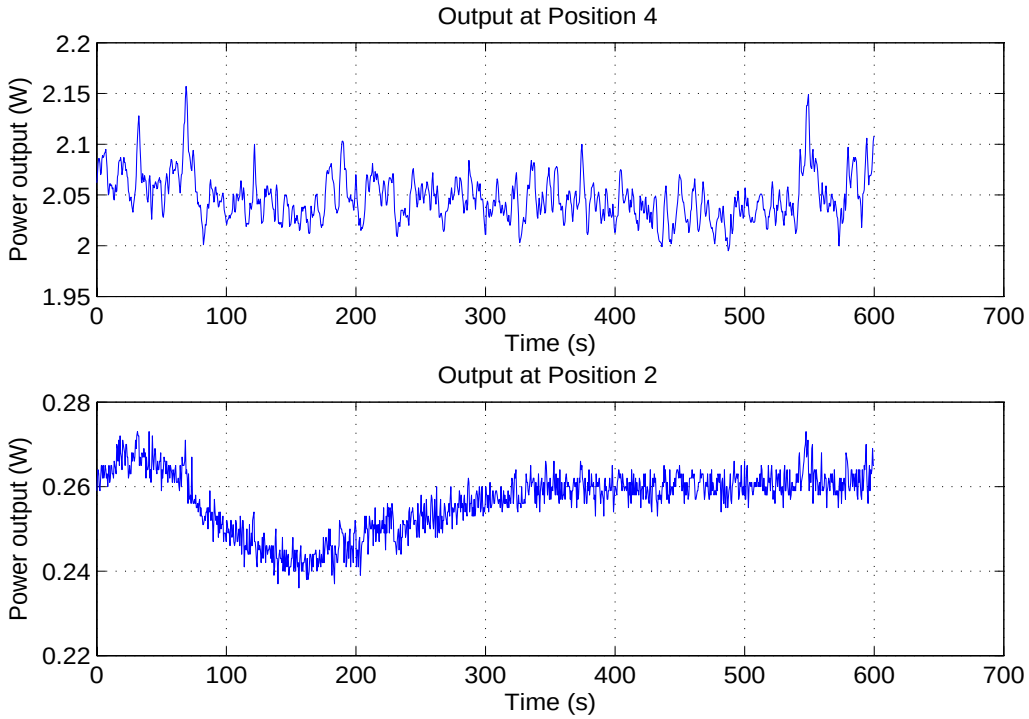

Figure 4.10. Measured output power. The pump current is held at $I_p = 18$ A for $t = 300$ s and then increased to $I_p = 20$ A and performing the same measurement.

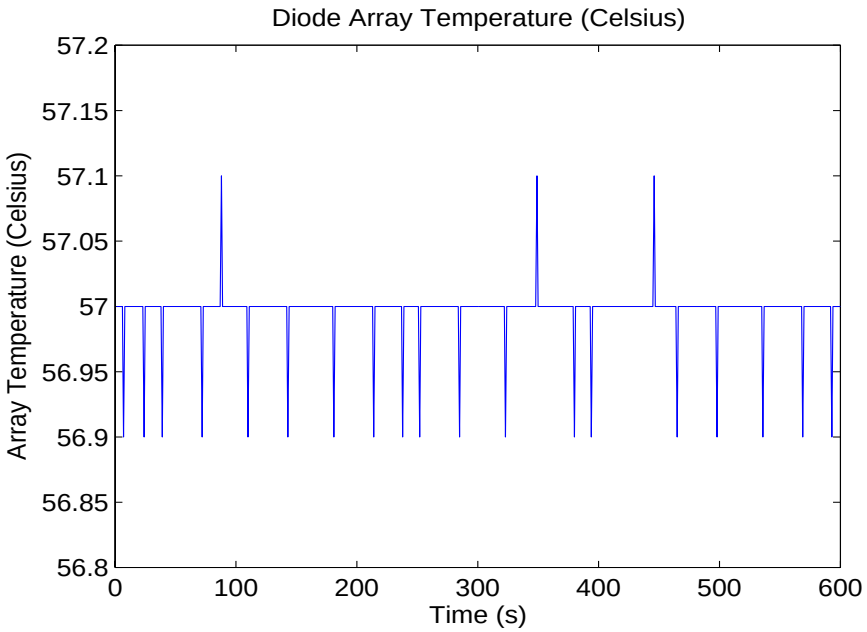

Figure 4.11. Pump diode temperature, measured during the first power measurement.

The variation in output power was higher at mirror 2 than at mirror 1, until some thermal equilibrium was reached. This can be explained by the fact that the two mirrors used were different. Mirror 1 is fabricated to transmit 75% of the fundamental Nd:YAG wavelength at $\lambda = 1064\,\text{nm}$. Mirror 2 is a dichroic mirror designed with a multilayer coating to transmit and reflect selectively depending on wavelength. A spectra of mirror 2 is shown in figure 4.12.

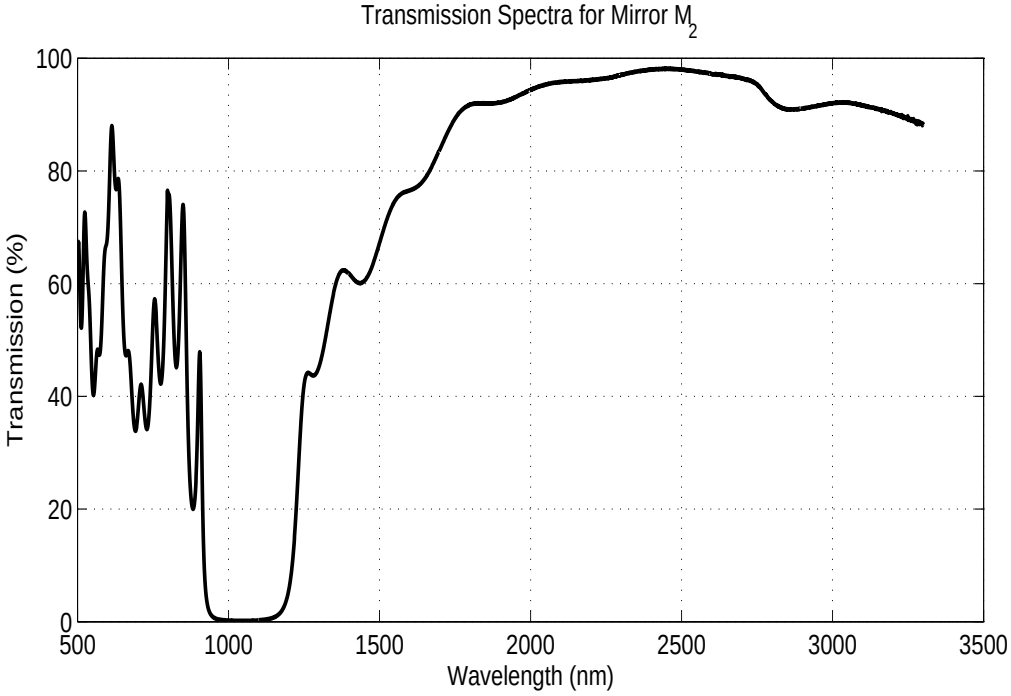

Figure 4.12. Dichroic spectra for the mirror M_2 in figure 4.7. Measurement done by A. Eriksson, FOI.

At $\lambda = 1064\,\text{nm}$ the transmission for the dichroic mirror is low, but not ideally zero. If a part of the transmitted radiation was absorbed in the coatings of the dichroic mirror, then this will in turn affect the transmission curve as a function of temperature. The effects of a variation in the order of 0.1% in a 1% transmission would be seen more easily than a variation of 0.1% in a 25% transmission. After reaching the thermal equilibrium for the coated material, the transmitted power stabilized. For mirror 1, the absorption in the coatings seemed to be less compared to mirror 2. Even with an output variation in power at mirror 2 this has very little effect on the internal intensity. The variations will however affect the focal length method used previously.

The measurements have only been done with an output coupling mirror reflectivity of 75%. By using a mirror with higher reflectivity, the internal intensity will grow according to equation (3.1) which is also plotted in figure 4.13.

The fraction of absorbed radiation in the dichroic mirror coatings will therefore increase. A larger absorption in the coatings will affect the amplitude of fluctuations seen in the output power at mirror 2, however the time until reaching a thermal equilibrium would be the same. Larger absorption will only increase the

equilibrium temperature but not the time reaching it.

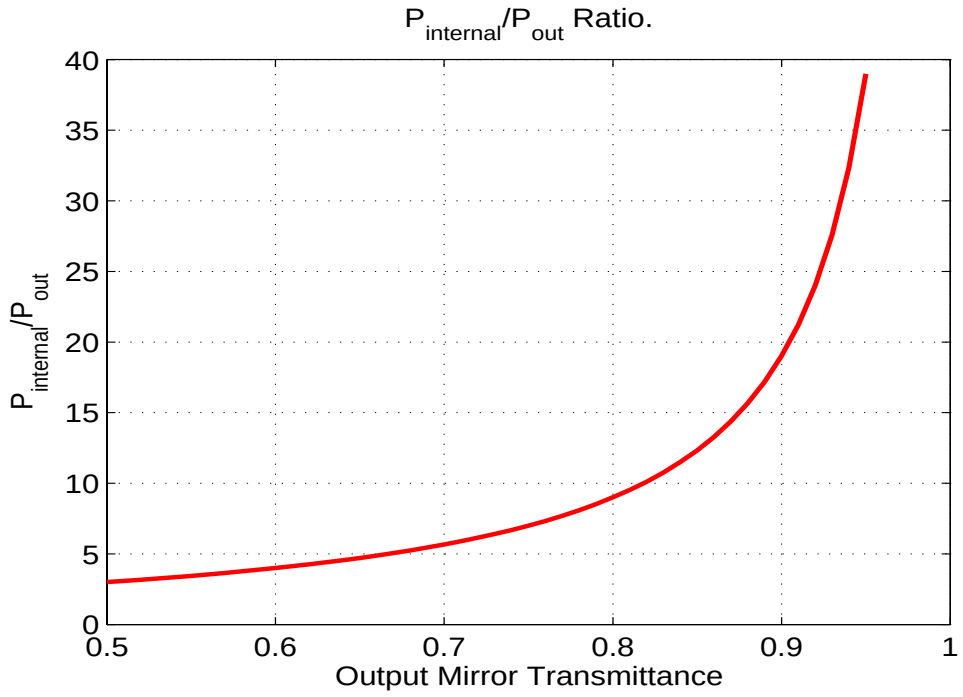

Figure 4.13. Plot of equation (3.1), showing the ratio of output power versus internal power $P_{internal}/P_{out}$ as a function of mirror 1 transmittance.

4.3 Optical Parametric Measurements

4.3.1 Component Placements

When introducing the Q-switch and the separate OPO cavity [mirror M_3 and M_4 in figure 3.1] for the KTP crystal, the complexity of the system increases. It is important for an efficient conversion of the Nd:YAG radiation that the pulses are stable. Depending on the choice of pulse repetition frequency and alignment of the components, phenomena such as double pulsing or even triple pulsing have been noticed. It is important to optimize the system so that these problems are avoided.

The OPO cavity was placed as close to mirror M_2 as possible, since for a plane-plane cavity the waists are located on the mirror surfaces of M_1 and M_2 [7]. The OPO cavity length was chosen as short as possible (~ 2.5 cm), but still long enough to be able to adjust the angle of the crystal in the copper holder. The temperature controller was set to hold a constant temperature at 40 °C for the copper holder to minimize the fluctuations in converted output power. This specific temperature was chosen, since it turned out that the temperature of the heat sink could reach as high as $50 - 55$ °C after a couple of hours. The thermoelectric elements cannot effectively cool the crystal below this temperature after running

the laser continuously for a longer period of time. The mirror M_5 with same characteristics as M_2 was introduced in order to filter out the small amount of Nd:YAG radiation transmitted by M_2. This was done to ensure that only the converted signal and pump wavelengths were measured at position 2.

As mentioned above, it is important to reach the working temperature for all parts before optimizing the system. A fixed pump current was chosen for a specific cavity length and this current was chosen as large as possible without making the cavity unstable. The analysis done in section 2.3.4 only considered one internal lens. When introducing the Q-switch with two internal silica crystals together with mirrors M_3 and M_4 and the KTP-crystal, these elements need to be included in a stability analysis. This is hard to do theoretically, so the method is to simply analyze different cavity lengths and notice which one provides the best result in converted output power and stability.

From all the resonator setups tested, the best results were obtained for those with a symmetric setup, i.e. with the laser module placed in the middle of the cavity as shown in figure 3.1. A number of symmetric and nonsymmetric setups were tested, and the results are summarized in figures 4.14, 4.15 and 4.16.

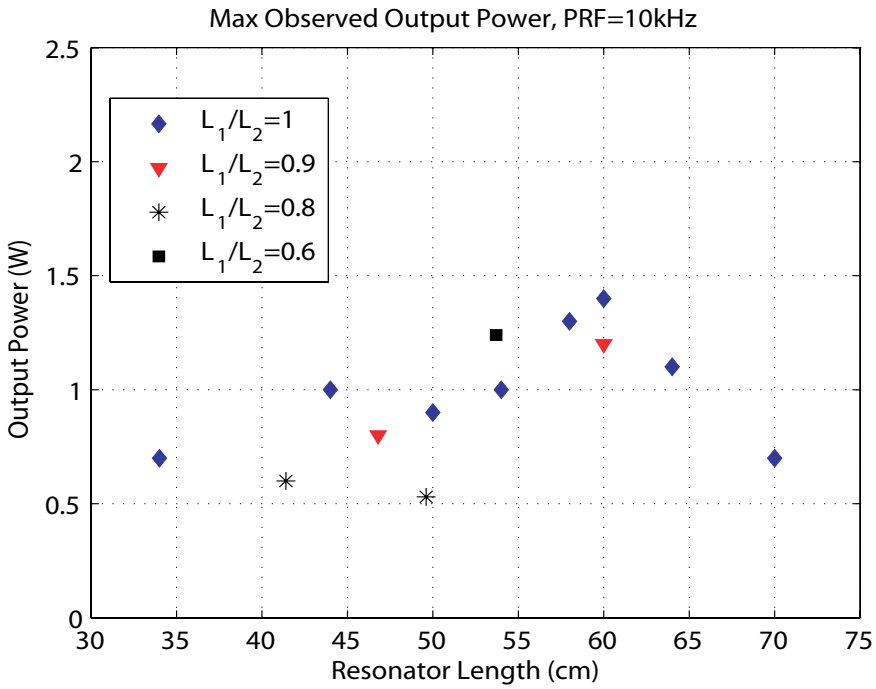

Figure 4.14. Highest observed converted output power measured at position 2, for different cavity setups. PRF=10 kHz.

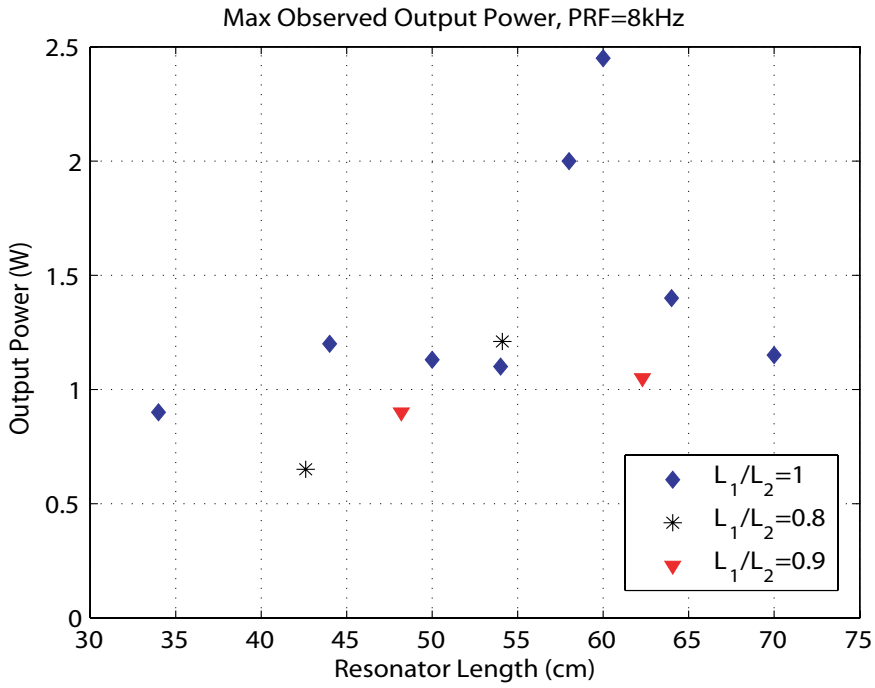

Figure 4.15. Highest observed converted output power measured at position 2, for different cavity setups. PRF=8 kHz.

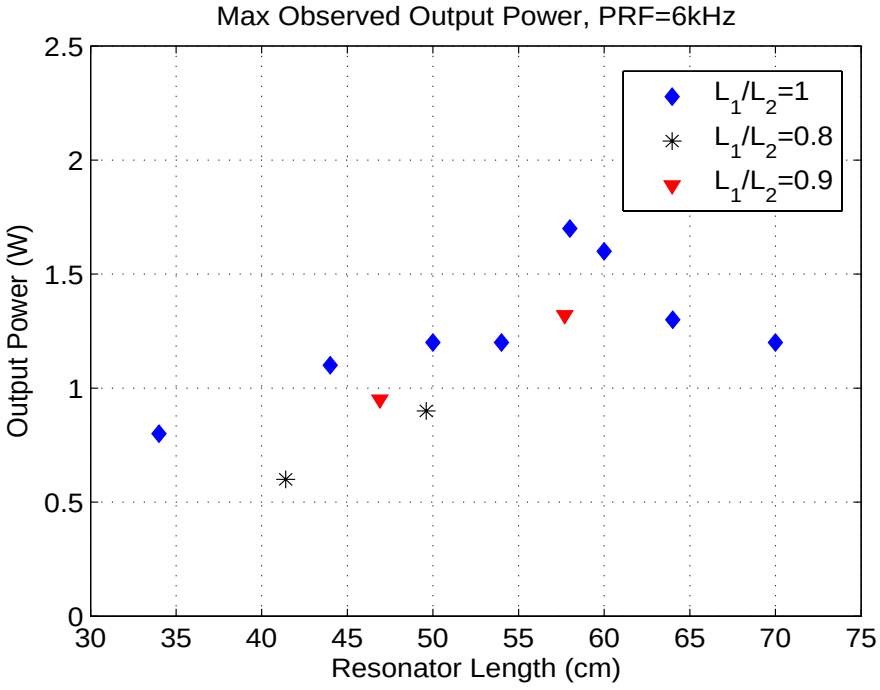

Figure 4.16. Highest observed converted output power measured at position 2, for different cavity setups. PRF=6 kHz.

The ratio of L_1 and L_2 show the relation between distances used [see figure 4.7] and so the total length of the resonator is $L = L_1 + L_2$. For non symmetric setups, the ratio $L_1 < L_2$ was chosen, in order to be able to fit the OPO cavity part successfully. Another reason was that the optical elements cannot be placed freely on the mounting table. So in order to use a symmetric/nonsymmetric cavity with the OPO cavity placed near mirror M_2, limits the choices of lengths between the components.

At each of the symmetric setups, the pulse repetition frequency was changed to see the effect on the converted output power. From figures 4.14, 4.15 and 4.16 the maximum output power of converted radiation from the parametric oscillator was $P_{OPO} \approx 2.5$ W at $L = 60$ cm with a PRF=8 kHz. The pump current to the system was $I_p = 23.2$ A. The converted output power fluctuated between $2.0 - 2.5$ W for about 20 seconds until it dropped down to around $1.3 - 1.5$ W. Due to fluctuations in the converted power, a constant re-optimization had to be manually done with the tip-tilt knobs for the OPO cavity mirrors M_3 and M_4. This suggested that there were instabilities due to thermal effects in the added components in the resonator.

Since the best result was achieved for the symmetric $L = 60$ cm, this cavity was used in all the remaining measurements.

4.3.2 Pulse Measurement

The pulses were measured using two photo diodes placed near the detector at position 1 and the detector at position 2 in figure 3.1. The pulse stability for the OPO was found to be most stable for a PRF=6 kHz. It was also noticed that the fluctuations of the converted OPO power seemed to decrease compared to using PRF=10 kHz and PRF=8 kHz. Even if the highest output power was achieved at PRF=8 kHz, also seen in figure 4.15, the long term stability was improved by decreasing the pulse repetition frequency. This can be explained from the fact that using a lower PRF will allow the laser to buildup a larger pulse which results in a more stable conversion in the KTP-crystal. The pulses are seen in figure 4.17 and 4.18.

From figures 4.17 and 4.18 several interesting features can be observed. Firstly the pulse length for the OPO-pulse is shorter than the Nd:YAG pulse. An explanation for this can be done with equation (2.39), section 2.6, in mind. The conversion is started when the intensity for the Nd:YAG pulse is greater than the threshold current. The fast rise time for the OPO pulse seen in figure 4.18 is also an indication of this. When the intensity is high enough to overcome the threshold, the OPO pulse is built up very fast. Two different coaxial cables were used to measure the pulses and this affects the time when the OPO pulses are registered relative to the Nd:YAG pulses. The pulse width for the Nd:YAG is approximately $\tau_p \approx 60$ ns at full width at half maximum (FWHM). FWHM is the distance between points on the curve at which the function reaches half its maximum value. For the OPO pulse the width is approximately $\tau_p = 30$ ns at FWHM. Most of the time the number of OPO pulses varied meaning that not every pump-pulse was converted in the KTP-crystal. One explanation for this is the sensitivity of

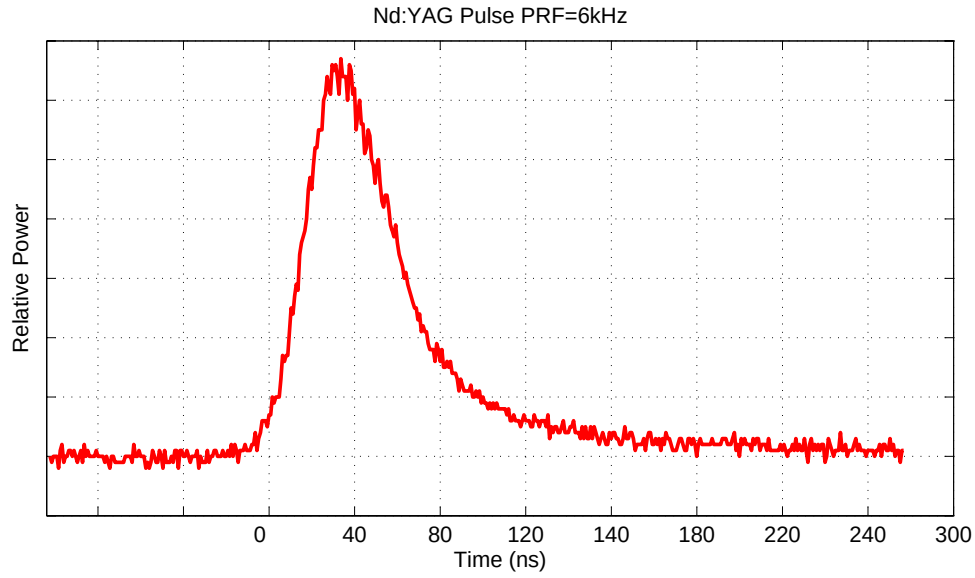

Figure 4.17. Pulse evolution from the Nd:YAG, with a PRF=6 kHz at $I_p = 23.2$ A. The pulse width is approximately $\tau_p \approx 60$ ns at FWHM.

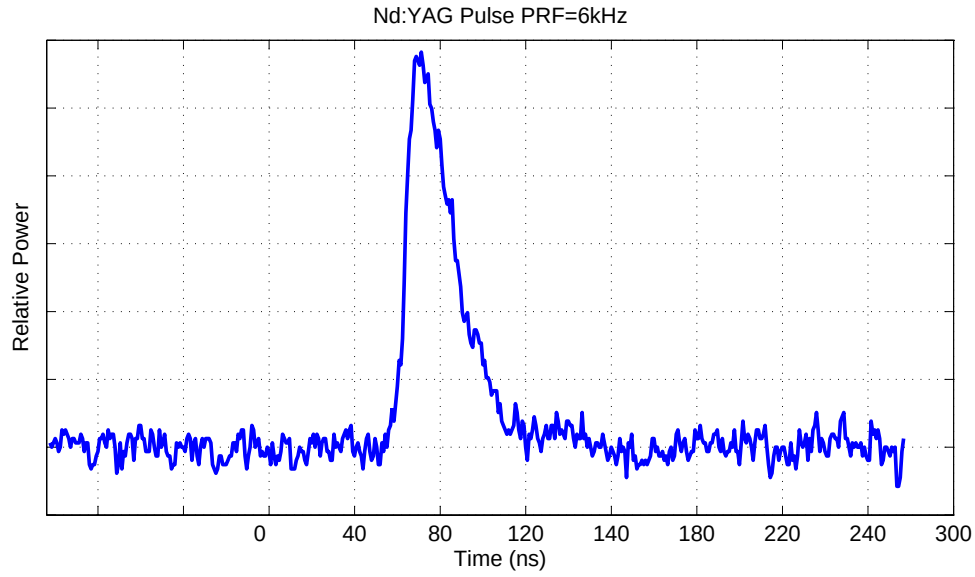

Figure 4.18. Pulse evolution from the OPO-pulse around $\lambda = 2\mu$m, with a PRF=6 kHz at $I_p = 23.2$ A. The pulse width is approximately $\tau_p \approx 30$ ns at FWHM.

the doubly resonance condition. Since the energy transfer between all three waves are related by their relative phases [see the coupled wave equations (2.35) section 2.5.4], the conversion is sensitive to the length of the OPO cavity.

The mirrors M_3 and M_4 were observed to absorb radiation since the mirror holders could reach as high as $45 - 50\,^{\circ}$C when running the system for about 3 hours. The absorption seemed to be higher for M_3 compared to M_4. Mirror M_3

also received optical damage in the coatings. The damage was a result from either a larger absorption of the Nd:YAG radiation in the coatings of this mirror, and/or that a focus was produced near or on the mirror surface. In a complex system like this, several internal waists can exist since all added components can act as internal lenses. Depending on the individual placements of the components, these waists will be located at different positions.

Naturally the conversion will be directly affected by the temperature fluctuations of these mirrors. This was one explanation why the OPO cavity always required re-optimization in order to "balance" out the modifications that were done to the OPO cavity due to curvature changes in the mirrors.

4.3.3 Converted OPO Power Stability

The stability of the converted output power was analyzed. The result is presented in figure 4.19. As can be seen from figure 4.19 the variations are rather large. As a

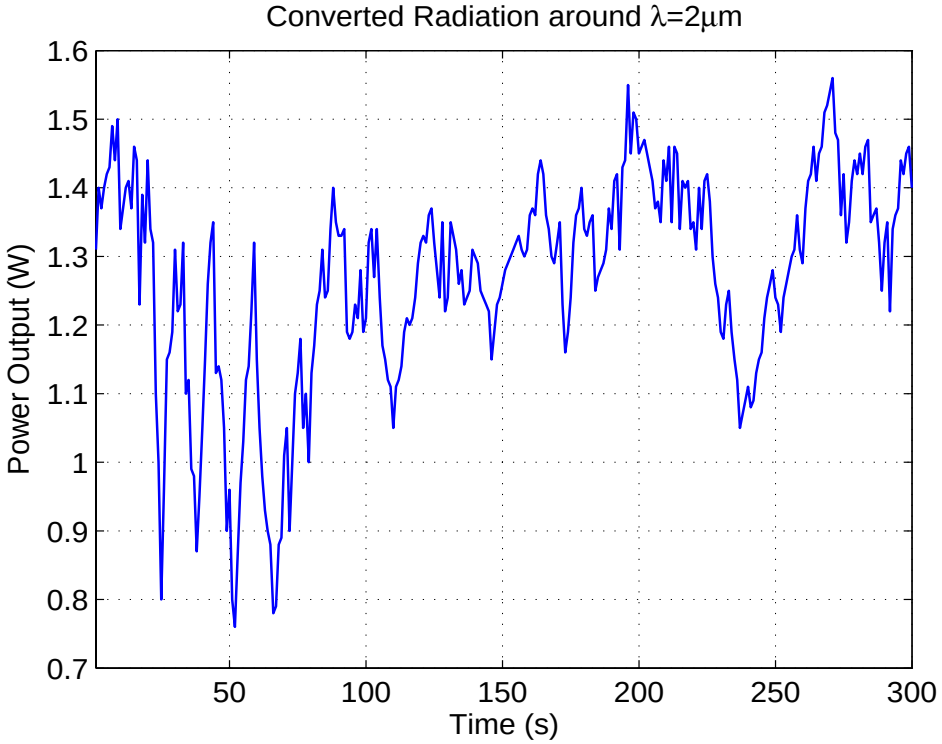

Figure 4.19. Converted output power from the KTP-crystal. Measured time was $t = 300\,\mathrm{s}$. Pump current $I_p = 23.2\,\mathrm{A}$, Temperature controller $T_c = 40\,^{\circ}\mathrm{C}$.

comparison, the converted output power was measured using a non-cooling crystal holder. The Nd:YAG radiation transmitted by M_2 was measured at position 3 and the converted OPO power at position 2 in figure 3.1. The result is presented in figure 4.20.

Figure 4.20 clearly shows the problematic behavior when the cooling of the crystal is absent. When the temperature of the crystal increases, the heat gradients

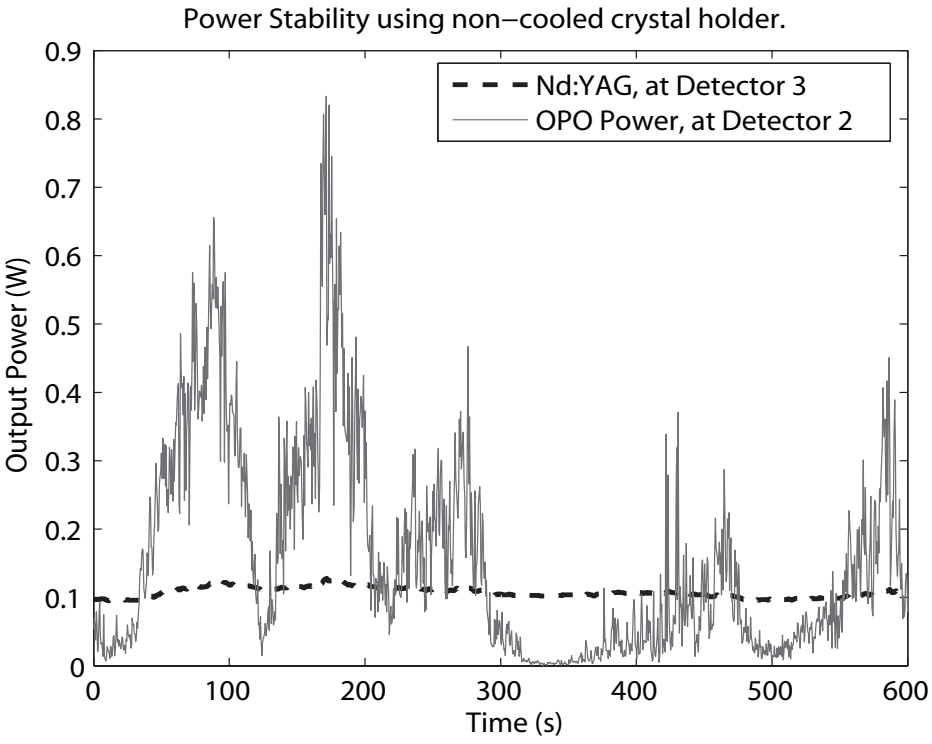

Figure 4.20. Converted output power from the KTP-crystal with no temperature controlling. Measured time was $t = 600\,\mathrm{s}$. Pump current $I_p = 23.2\,\mathrm{A}$.

cause strains in the KTP crystal changing the stability and the phase matching requirement for successful conversion. Sometimes the converted OPO output power drops down to zero watts while Nd:YAG power keeps stable throughout the measurement.

The conclusion is that cooling of the KTP crystal is an important part to stabilize the OPO process. However, even when the crystal is kept at a constant temperature, fluctuations still exist as can be seen from figure 4.19.

Since it was observed that M_3 and M_4 apparently absorbed a considerable amount of heat, the temperature of the mirror holders were measured with an IR temperature sensor. Due to the small length of the OPO cavity, it was difficult to measure directly on the mirrors. The IR sensor had an accuracy of $\pm 2\,^{\circ}\mathrm{C}$. The result is presented in figure 4.21.

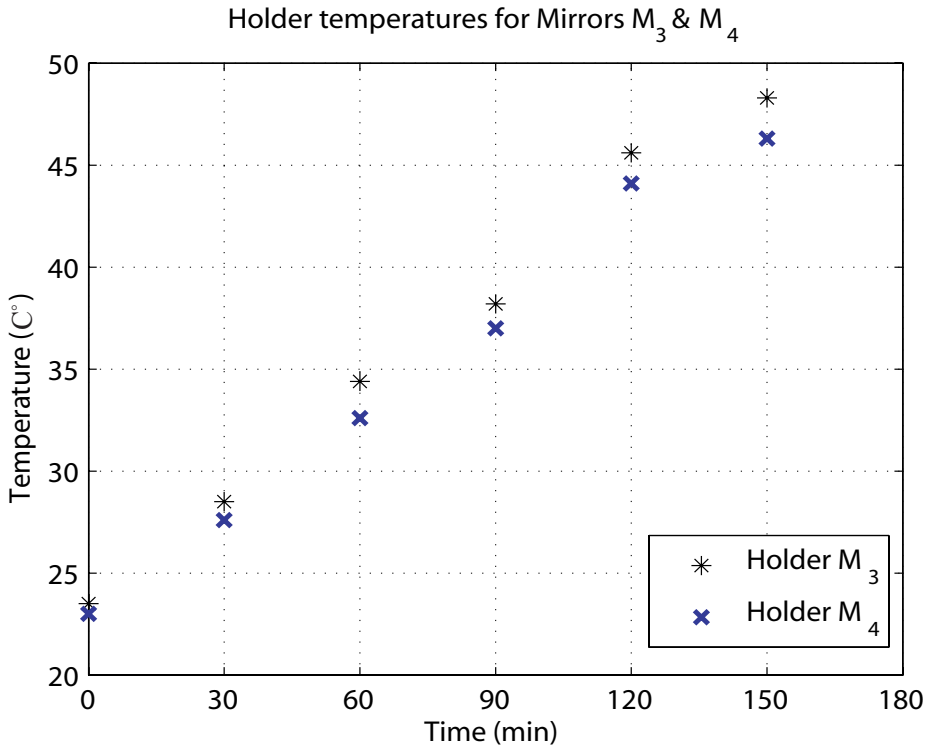

Figure 4.21. Mirror holder temperatures for M_3 and M_4 measured with an IR-Thermometer.

This mirror temperature measurement were performed over a 2.5 hour time period. The pump current varied when temperatures were taken, since other measurements were carried out simultaneously. The result show a rather large absorption in the OPO cavity mirrors running the system for a longer period of time. From this graph, it is difficult to say if the temperatures will stabilize over time, however, this is most likely.

During the OPO experiments, green laser light was also observed. This suggests that there is a second harmonic generation SHG process [see section 2.5.2] in the substrates of the mirrors, made of CaF_2. This can also be done with a nonlinear material such as KTP, but the crystal is then cut in a different direction in order to optimize for SHG generation. The green light produced was observed both with and without the KTP crystal present. The intensity was larger when the crystal was present. This observation indicates that a nonlinear effect takes place in the coatings of the mirrors, doubling the frequency of the Nd:YAG radiation which produce the green light.

4.3.4 Wavelength Tuning

To measure the wavelengths of the signal and idler, a spectrum was taken with a grating monochromator. The OPO cavity was optimized to ensure that the converted power did not vanish during the monochromator scan. The result is presented in figure 4.22[A]. The corresponding linewidth is depicted in figure 4.23.

From figure 4.22[A] the signal wavelength is located at $\lambda_s = 1960\,\text{nm}$, and the

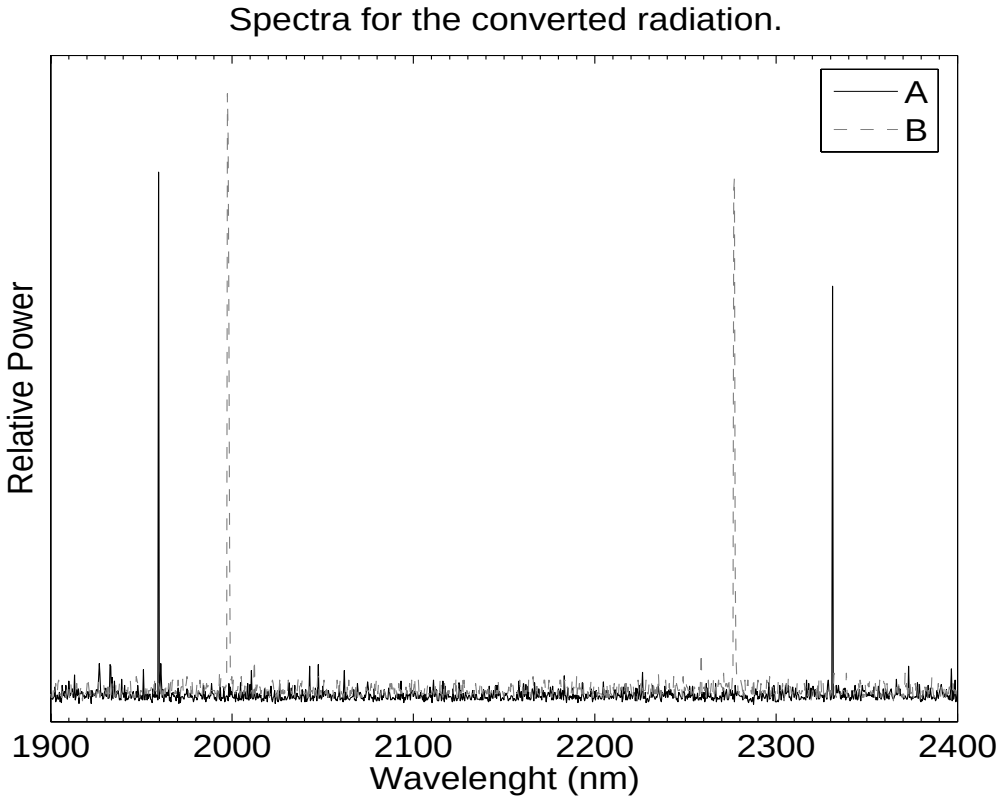

Figure 4.22. Spectra showing the signal and idler wavelengths. Rotation of crystal produces new wavelengths as shown in [B].

idler $\lambda_i = 2331\,\text{nm}$. The signal wavelength indicates, that the angle difference is nearly 2.5° above the degeneration angle 51.4° at $\lambda_s = \lambda_i = 2128\,\text{nm}$, see figure 2.17 in section 2.7.2.

The peak difference of the signal versus idler wavelengths stems from the fact that the photon intensity was different for the signal and idler. It is also possible that the signal and idler were not perfectly collinear incident on the monochromator resulting in a slight difference of intensity. Another reason is that the transmission in the optical elements used to collect the signal and idler onto the monochromator, was different for the two wavelengths.

By rotating the crystal, the phase matching condition for other wavelengths was fulfilled. Since the dimensions of the manufactured crystal holder limits applicable rotation of the crystal for small cavity lengths between mirrors M_3 and M_4, the un-cooled crystal holder was used in the measurement. This will make the measurement cumbersome, since previous experiments with this un-cooled holder sometimes resulted in power drops down to zero watts, see figure 4.20. The result is presented in figure 4.22[B].

The spectrum 4.22[B] consists of two measurements, one from $\lambda = 1900 - 2250\,\text{nm}$ and the second from $\lambda = 2250 - 2400\,\text{nm}$. This was done since the idler was absent in repeated measurements with the monochromator. This was due to

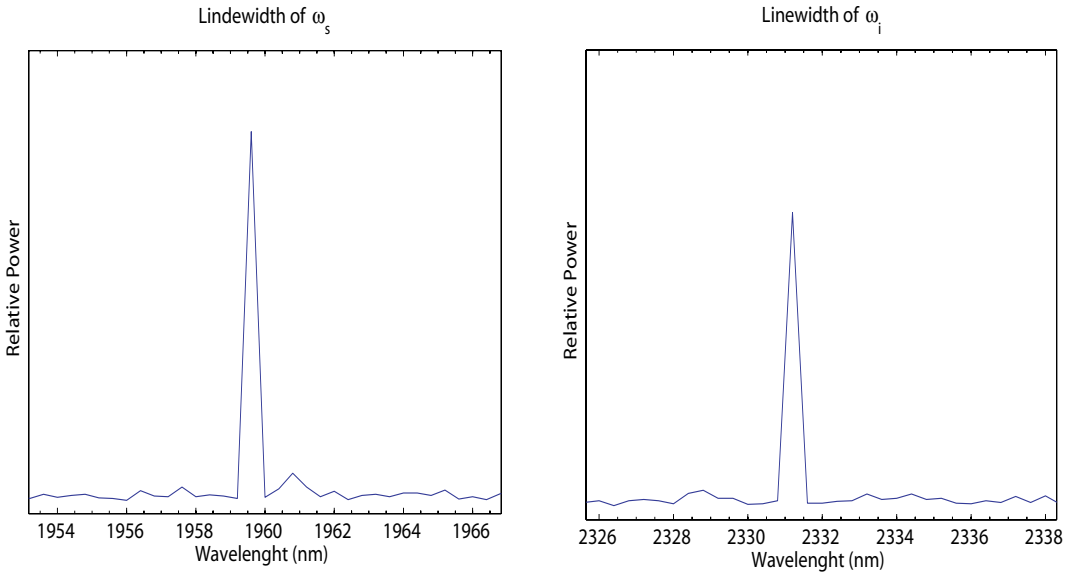

Figure 4.23. Linewidth of the signal (a) and idler (b) wavelengths.

power drops in converted output power using the non-cooled crystal holder. The second part of the measurement was therefore started from $\lambda = 2250 - 2400$ nm in order to find the idler wavelength. From figure 4.22[B] the wavelengths for the signal and idler now are $\lambda_s = 1998$ nm and $\lambda_i = 2277$ nm. Again looking at the phase matching plot 2.17, we see that this corresponds to a angle difference of 2° below the angle for degenerate phase matching.

4.3.5 Singly Resonant Result

By replacing mirror M_3 in figure 3.1 with a mirror that has high reflectance only for the signal, a stability increase in the output power was expected. In general singly resonant configurations are preferred, since they are more robust to cavity changes. In the singly resonant case only two waves enter the KTP crystal and the phase of the third wave will automatically adapt to optimize the conversion.

The dimensions of the singly resonant mirror was about half the thickness of the doubly resonant mirror previously used. Starting the conversion with this mirror turned out to be a real challenge, as expected due to the higher threshold. The few times when the OPO started converting radiation, the fluctuations were so large that the output power rarely became larger than 100 mW. This contradicts the theory discussion. An explanation for this behavior could be that the heat gradients in a thin mirror compared to a thick mirror changes more rapidly. This will cause larger fluctuations for the singly resonant case, and consequently harder to fulfil the phase matching condition. As a result the output power will fluctuate, and the rapid changes are hard to manually compensate by adjusting the tip-tilt knobs for the OPO cavity mirrors. This configuration was for this reason not analyzed further.

Chapter 5

Discussion and conclusions

An intracavity optical parametric oscillator has been studied. The thermal lensing of the rod was measured using two methods. Method I showed a reasonable description of the refractive power and an approximate value of the efficiency factor. The factor describes a ratio between the electrical input power from the diodes and the actual absorption of this power to the rod. An efficiency factor $\eta \approx 40\%$ was obtained which is a difference by a factor 2 compared to the theoretically estimated value $\eta \approx 19\%$.

Method I was cumbersome, since locating the focal point was done manually with a HeNe laser and a knife-edge. Since the laser produced two focal points due to the thermal induced birefringence, the measured values were approximated as the mean value of these two focal lengths. Another explanation regarding the difference in result is simply that the absorption in the rod was higher than expected. As shown, high absorption of heat in the rod will cause changes in refractive index and consequently large refractive powers of the rod.

Method I described how the refraction depended on the electrical input power when no laser radiation was generated. A second method was therefore tested. Method II gave two different values of the efficiency parameter depending on the polarization used in the calculation. The values were $\eta \approx 37\%$ for the azimuthal polarization and $\eta \approx 47\%$ for the radial polarization. These values were compared to the theoretical estimated value $\eta \approx 14\%$, and again showed a significant difference in result compared to the theoretical value. This method relied on the fact that the power drop was measured at the point where the resonator was critically stable. If the power dropped before this point due to other problems in the system, then Method II will not give an accurate description of the thermal lensing. The calculated values regarding the threshold current of the laser diodes were compared between the two methods. This indicated that the value $\eta \approx 37\%$, using the azimuthal polarization, gave the best result in Method II.

Further analysis of the behavior of the rod should be done as a step towards a better description of the laser system. This could include a numerical model of the thermal behavior of the Nd:YAG rod, or refining the methods used.

The output stability was measured, and the conclusion was that the power

output through the dichroic mirror stabilized after approximately 300 s. It was also shown by increasing the current from 18A to 20A that it took another 300 s to stabilize the output power. The Method II measurement did not take this time into account, which could explain why the method gave different values in the efficiency parameter. One solution to the problem is to use the beam-sampler and perform the same measurements collecting data from the output power that kept stable. This measurement was not done due to the fact that the variation in the output power at the dichroic mirror was realized first after the measurements had been done. The measurements were also time consuming.

The maximum converted output power from the OPO was 2.5 W in the region $\lambda = 2\ \mu$m. The optimal cavity length and pulse repetition frequency used for the Q-switch, were found by analyzing a number of different cavity setups. The best results were obtained for symmetric setups of the cavity, placing the laser module in the middle of the pump-cavity. From the different PRF:s tested, the conclusion was that lower repetition rates in general gave better results considering the stability, compared to higher repetition rates. Lower PRF:s will increase the pulse intensity used for conversion, but also optical damage in components in the system, mainly to the OPO cavity mirrors. Lower PRF:s can also introduce double pulsing which is an unwanted side effect for successful conversion.

The long term stability for the converted power was improved by using a cooled crystal holder to keep the KTP crystal temperature constant. The internal cavity mirrors absorbed radiation, and this is one reason why the converted power fluctuations occurred in the system. In order to keep the conversion at maximum, the OPO mirrors had to be re-optimized manually at all times. When the converted output power seemed to be stable (within 10% fluctuations), this was only true during short periods of time. When the crystal cooler was used, the power never dropped to zero watts after optimizing the OPO cavity.

When the singly resonant case was tested, the temperature of the mirror holder of M_3 was significantly lower compared to using the doubly resonant mirror. Even with this fact, using the SR mirror did not stabilize the converted power output compared to the DR case. The variations in output power above threshold is probably due to the thickness of the SR mirror. A slim mirror compared to a thick will cause rapid changes of the thermal gradients affecting the phase matching condition.

A small absorption of the pump, signal and idler existed in the crystal. This resulted in an induced thermal phase mismatch and lensing of the crystal, much like the lensing in the Nd:YAG rod. The thermal stresses in the KTP crystal will introduce a variation in the ordinary and extraordinary refractive indices used in the phase matching, and this variation degraded the performance of the conversion. A new crystal with higher quality which in turn equals less absorption, could resolve the problem.

Since the OPO cavity is small ($\sim$ 2.5 cm), the heat absorbed in the mirrors and the KTP-crystal will spread between the internal cavity components, after running the laser for a longer period of time. This is problematic since the crystal will absorb heat from the mirrors leading to difficulties in cooling it. This in turn leads to an increase in temperature for the crystal which now start to change the

phase matching condition with the result in significant drops in output converted power. When the cooling of the crystal fails, the whole system needs to be shut down in order to let the components cool down. The absorption problem has to be solved in order to be able to run the laser continuously with an efficient conversion. Active air cooling of the mirror holders is difficult, since the cavity must be kept free from dust particles. Instead new mirrors with less absorption should be considered.

The thermally induced birefringence in the rod complicates the use of polarized laser radiation for pumping the OPO. The birefringence "scrambles" the use of linear polarization passing through the rod. The KTP crystal uses only one polarization direction in the type-II conversion, since e$\rightarrow$ o+e, see section 2.7.2. The conversion efficiency is therefore limited due to the induced birefringence effects. Attempting to use a polarizer internally in the laser cavity will most likely cause high losses and diminished output power so this was not tested. Compensating for this birefringence effect is not a simple task. One solution is to use another pumping source, such as Nd:YALO, which do not show the thermally induced birefringence effects. A generated output up to 21 W of 2 μm radiation was reported by R.F. Wu *et al.* [20], using the Nd:YALO laser.

To summarize, improving the conversion results from the intracavity optical parametric oscillator should include the following.

- Replacing the pump source. Nd:YALO would be a good candidate, without the induced birefringence effects.
- New KTP crystal with higher quality to avoid absorption of the wavelengths.
- New OPO cavity mirrors that do not absorb as much radiation as the mirrors currently used.
- To be able to place the crystal as close to the beam waist as possible, one should replace the mirror M_4 with a mirror that in addition is highly reflective at the Nd:YAG wavelength. This would mean that the rear mirror M_2 could be removed, and the distance from the KTP crystal to the waist located on the rear pump-cavity mirror would be shortened.
- A folded cavity scheme producing a small waist incident on the KTP crystal, could improve the conversion process.
- A better model of the thermal lensing will provide means for calculating an optimal length and mirror configuration to produce a small beam waist incident on the KTP crystal.

Bibliography

[1] F. L. Pedrotti and L. S. Pedrotti. *"Introduction to Optics"*. Prentice-Hall International, first edition, 1996. ISBN 0-13-016973.

[2] J. T. Verdeyen. *"Laser Electronics"*. Prentice Hall, third edition, 2000. ISBN 0-13-706666-X.

[3] W. Koechner. *"Solid-State Laser Engineering"*. Springer-Verlag, Berlin, Heidelberg, fourth edition, 1996. ISBN 3-540-60237-2.

[4] L. Råde and B. Westergren. *"Mathematics Handbook"*. Studentlitteratur, Lund, fourth edition, 1998. ISBN 91-44-00839-2.

[5] N. Hodgson and H. Weber. *"Optical Resonators, Fundamentals, Advanced Concepts and Applications"*. Springer-Verlag London, first edition, 1997. ISBN 3-540-76137-3.

[6] O. Svelto. *"Principles of Lasers"*. Plenum Press New York, fourth edition, 1998. ISBN 0-306-45748-2.

[7] H.P. Kortz, R. Iffländer, and H. Weber. *"Stability and Beam Divergence of Multimode Lasers with Internal Lenses"*. *Appl. Opt.*, vol. 20, no. 23, pp. 4124-4134, 1981.

[8] D.L. Mills. *"Nonlinear Optics, Basic Concepts"*. Springer-Verlag, Berlin, Heidelberg, second edition, 1998. ISBN 3-540-64182-3.

[9] W. Ubachs. *"Non Linear Optics"*. Lecture Notes, Laser Centre Vrije Universiteit Amsterdam, Department of Physics and Astronomy, 2001. URL: `http://www.nat.vu.nl/~wimu/NLO-2001.pdf`

[10] N. P. Barnes. *"Optical Parametric Oscillators"*, in F.J. Duarte, *"Tunable Lasers Handbook"*, pp. 293-348. Academic Press Inc. London, first edition, 1995. ISBN 0-12-222695-X.

[11] J. Hellstrom. *"Nanosecond Optical Parametric Oscillators and Amplifiers based on Periodically Poled $KTiOPO_4$"*. PhD thesis, Royal Institute of Technology, Stockholm, Sweden, 2002. ISSN 0280-316X.

[12] N. Boeuf, I. Branning, E Chaperot, S. Dauler, G. Guérin, A. Jaeger, A. Muller, and A. Migdall. *"Calculating Characteristics of Noncollinear Phase Matching in Uniaxial and Biaxial Crystals"*. *Opt. Eng.*, vol. 39, pp. 4124-4134, 2000.

[13] F.A. Hopf and G.I. Stegeman. *"Applied Classical Electrodynamics, Volume II: Nonlinear Optics"*. John Wiley & Sons, Inc., second edition, 1986. ISBN 0-471-82787-8.

[14] A.V. Smith. Snlo nonlinear optics code. MS 1423, Albuquerque, NM 87185-1423. URL: `http://www.sandia.gov/imrl/XWEB1128/xxtal.htm`.

[15] M. A. Heald and J. B. Marion. *"Classical Electromagnetic Radiation"*. Saunders College Publishing, third edition, 1995. ISBN 0-03-097277-9.

[16] L. R. Marshall. *"Laser Diode-pumped Solid State Lasers"*, SC129 Short Course Notes, in *Conference on Lasers and Electro-Optics, CLEO 2002*. Long Beach California, 2002.

[17] *"Cutting Edge Optronics, application notes"*. Technical report, 2005. URL: `http://www.st.northropgrumman.com/ceolaser/SiteFiles/docs/PDFs/Typical_RB_Series_Performance_info.pdf`.

[18] L. Qiang, Z. Wang, and T. Zuo. *"A method measuring thermal focal length of all rays polarized in radial and tangential direction of high power Nd:YAG laser"*. *Opt. Comm.*, vol. 35, pp. 155-158, 2004.

[19] N. Pavel, T. Dascalu, and V. Lupei. *"Stable Resonators for Fundamental Mode Operation"*. *Opt. Eng.*, vol. 35, no. 5, pp. 1239-1246, 1996.

[20] R.F. Wu, P.B. Phua, K.S. Lai, Y.L. Lim, Ernest Lau, Audrey Chng, Christophe Bonnin, and Dominique Lupinski. *"Compact 21-W 2-μm Intracavity Optical Parametric Oscillator"*. *Opt. Lett.*, vol. 25, no. 19, pp. 1460-1462, 2000.

Appendix A

Inversion and the 4-level system

In order to describe the rate equations of the 4-level system, the basic equations describing the different processes in figure 2.1 must be written down. For stimulated absorption we have [2]

$$\left(\frac{\partial N_2}{\partial t}\right)_{abs} = +B_{12}N_1\rho(\nu) = -\left(\frac{\partial N_1}{\partial t}\right)_{abs}. \tag{A.1}$$

The coefficient B_{12} is a constant characteristic of the atom, and $\rho(\nu)$ is the energy density [2], so the ratio $B_{12}\rho(\nu)$ can be interpreted as the probability per unit frequency that transitions occur as an effect of the external field.

Spontaneous emission can be described by

$$\left(\frac{\partial N_2}{\partial t}\right)_{spont} = -A_{21}N_2 = -\left(\frac{\partial N_1}{\partial t}\right)_{spont} \tag{A.2}$$

where the coefficient A_{21} is the *radiative rate*.

Stimulated emission is described by

$$\left(\frac{\partial N_2}{\partial t}\right)_{stim} = -B_{21}N_2\rho(\nu) = -\left(\frac{\partial N_1}{\partial t}\right)_{stim}. \tag{A.3}$$

The Nd:YAG belongs to the class of 4-level laser systems, and a idealized energy level diagram[1] is shown in figure A.1. The parameter τ_2 is intended to be the effective lifetime of level 2. For successful laser generation we need to populate the upper energy level N_2 so that growth of the field due to stimulated emission is possible. The lifetime for an atom in this inverted state is in general extremely short ($\sim 10^{-8}$).

[1] In reality the 4-level system actually has many transition levels. Also the pump band may consist of several or a continuum of energy levels. For Nd:YAG the absorption ranges from $0.3-0.9\mu$m with strong absorption around $810nm$, resulting in a transition from ${}^4F_{3/2} \rightarrow {}^4I_{11/2}$ energy levels with $\lambda = 1064$ nm. [3]

Using for instance optical pumping, four transition levels occur, one being metastable with much longer lifetime ($\tau_2 \sim 10^{-3}$ s) than the other levels. This allows the creation of the desired population inversion $N_2 > N_1$, since the decay time τ_{10} is very short. Stimulated emission will now start the laser amplification process.

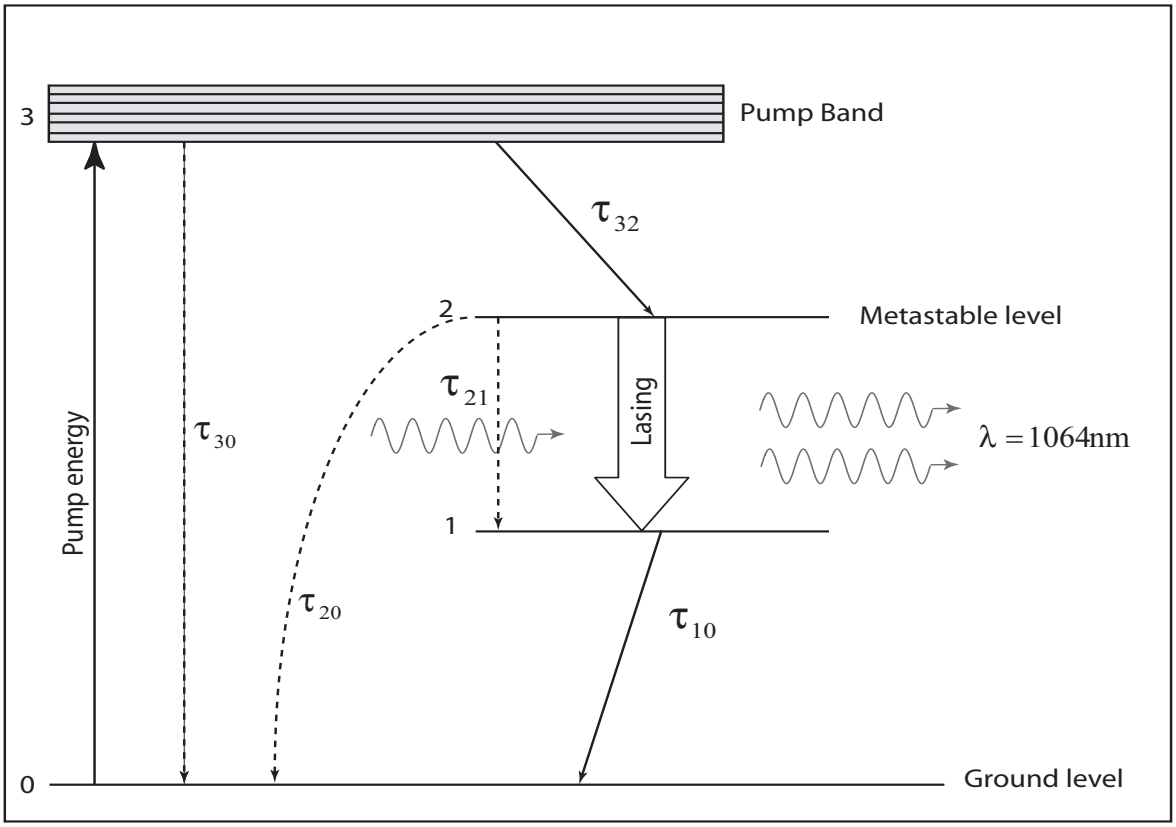

Figure A.1. The 4-level system for Nd:YAG.

From figure A.1 the basic laser rate equations can be written down using (A.1), (A.2) and (A.3) [6]

$$\left(\frac{dN_2}{dt}\right) = R_p - B\phi[N_2 - N_1] - \frac{N_2}{\tau_2} \tag{A.4a}$$

$$\left(\frac{dN_1}{dt}\right) = \frac{N_2}{\tau_{21}} + B\phi[N_2 - N_1] - \frac{N_1}{\tau_{10}} \tag{A.4b}$$

$$\left(\frac{d\phi}{dt}\right) = V_a B\phi[N_2 - N_1] - \frac{\phi}{\tau_c} \tag{A.4c}$$

The equations assume that τ_{32} is an extremely fast transition, so that the pump rate R_p can be seen working directly to the N_2 level.

The term ϕ represents the total amount of photons in the cavity. V_a is the mode volume in the in the Nd:YAG medium, and B is the stimulated transition rate per photon, per mode. The term $V_a B\phi[N_2 - N_1]$ therefore describes the increase of

photon population from stimulated emission. From equation (A.4c) it can be seen that positive growth is only possible if $N_2 > N_1$. The term ϕ/τ_c in equation (A.4c) accounts for the photon losses in the system, where τ_c is the photon lifetime in the cavity.

Both τ_{32} and τ_{10} are radiationless transitions, and these take place due to mechanical factors such as collisions or vibrations in the crystal lattice. There is always a threshold for the pump in order to achieve laser action, and above this the output power will increase linearly with pump power, providing that the resonator is stable.

Appendix B

ABCD matrices

The ABCD matrix formalism provides a systematic approach for ray tracing through individual optical elements, by describing each element in the system by a matrix. This method makes it possible to combine the individual matrices to a single *system matrix* which describes the reflections and refractions the ray experiences propagating through all elements in the system. This method can be used in the paraxial approximation, i.e. when the rays are assumed to propagate with small angles to the optical axis.

Each round-trip in an optical resonator can be described by an equal repetitive system called the equivalent lens-waveguide, where each mirror have been replaced by a lens with $f_n = \rho_n/2$.

Consider a system of $\mathbf{n}$ optical elements as shown in figure B.1.

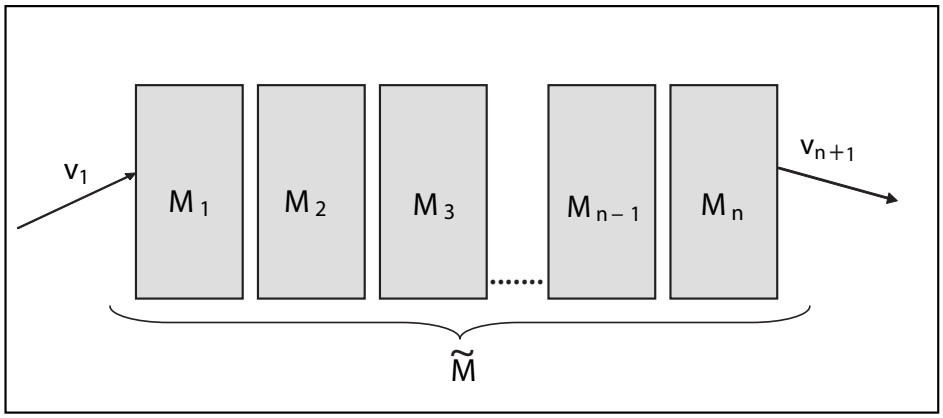

Figure B.1. Ray transfer scheme through n optical elements.

An incoming ray vector from the left $\mathbf{v}_1$ is then transformed by the first matrix $\mathbf{M}_1$ into the outgoing vector $\mathbf{v}_2$ by the relation

$$\mathbf{v}_2 = \mathbf{M}_1 \mathbf{v}_1 \tag{B.1}$$

where

$$\mathbf{v}_n = \begin{bmatrix} x_n \\ \alpha_n \end{bmatrix}. \tag{B.2}$$

The ray vector describes the starting point x, and the inclination angle α. Generalizing the above with $\mathbf{n}$ elements we have

$$\mathbf{v}_{n+1} = \mathbf{M}_n\mathbf{M}_{n-1}\mathbf{M}_{n-2}\ldots\mathbf{M}_2\mathbf{M}_1 = \begin{pmatrix} A & B \\ C & D \end{pmatrix}\mathbf{v}_1 = \widetilde{\mathbf{M}}\mathbf{v}_1 \tag{B.3}$$

so that the multiplication is performed in a descending order. For example, free space propagation a distance d together with a thin lens with focal length f as shown in figure B.2 results in the transfer matrix

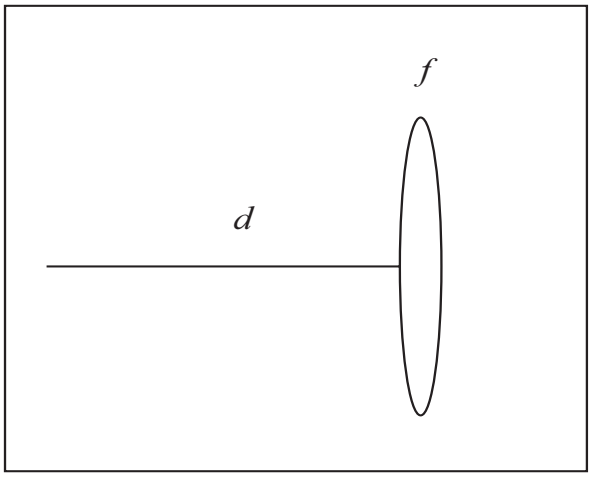

Figure B.2. Simple system using the ABCD propagation method.

$$\widetilde{\mathbf{M}} = \begin{pmatrix} 1 & 0 \\ -1/f & 1 \end{pmatrix}\begin{pmatrix} 1 & d \\ 0 & 1 \end{pmatrix} = \begin{pmatrix} 1 & d \\ -1/f & -d/f+1 \end{pmatrix}. \tag{B.4}$$

A comprehensive list of matrices for optical elements can be derived, see for instance [5].

Appendix C

Equipment

Mirrors:

- One 75% output coupling mirror, CVI Laser Corp.
- Three dichroic mirrors, Rocky Mountain Instr.

Detectors:

- Ophir-10000 W, water cooled power meter. Range $0 - 10000$ W.
- PM3 detector from Molectron Detector Inc. Range $0 - 3$ W.
- PM10 detector from Molectron Detector Inc. Range $0 - 10$ W.

Power meters:

- Molectron 5200, single channel power meter.
- Molectron EPM2000, dual channel power meter.
- Ophir Power Meter.

Photo Diodes:

- Alphalas UPD-300, rise time 300 ps. Silicon, range 320-1100 nm.
- Vigo Systems PEM-L-3, rise time ≤ 0.5 ns, Hg-Cd-Zn-Te, range 2-5 μm.

Laser Module:

- Cutting Edge Optronics RB30-2C2, diode pumped laser module.

Laser Driver:

- Cutting Edge Optronics, Model CEO2800.

Q-switch:

- Neos Technologies N33027-40-4-XY, water cooled acousto-optic Q-switch.

Temperature Controller:

- Marlow Industries Temperature Controller, Model SE5010.

Grating Monochromator:

- Digikröm 240, CVI Laser Corp.

IR-thermometer:

- Biltema Art.15-278, Range -50° to 538°. Accuracy ±2°.

Appendix D

Matlab Code

Calculation of the η factor using Method-I.

```
------------------------------------------------------------------
Calculation of the Efficiency factor, using Method I Measurements.
------------------------------------------------------------------

%Laser Data

K=0.14;              %Thermal Conductivity
beta=7.3e-6;         %dn/dT Temp. Derivative of index of refraction
alpha=7.5e-6;        %Thermal Coefficient of Expansion
Cr=0.017;            %Photoelastic Coefficient (radial component)
Cphi=-0.0025;        %Photoelastic Coefficient (tangential component)
n0=1.82;             %Index of refraction
r0=0.15;             %Radius of The laser rod
L=6.3;               %Length of the laser rod

A=pi*r0^2;           %Cross section of the rod.
R0=50;               %Curvature of the end faces of the rod at room temperature
V=34.1;              %Laser Driver voltage.

%Equation D=sigma*Pa+kappa;

kappa=-(2*(n0-1)/R0);

Ip=[25:-0.5:19];             %Pump current.
focal=[17.4330 18.6830 20.3330 21.2830 23.2330 24.6330 25.9330...
27.8330 29.7830 32.4830 35.4830 40.5830 46.2330];
                             %Measured Focal Lenght.
D=(1./focal);                %Refractive Power
```

```
Ith=9.4;                    %Threshold current diodes.
I=Ip-Ith;                   %Effective current
Peff=V*I;                   %Effective input power
Dtrue=D-kappa;              %True Refractive power to fit.
Z=polyfit(Peff,Dtrue,1);

sigma_r=(n0/(A*K))*(beta/(2*n0)+n0^2*alpha*Cr+((r0*alpha*(n0-1))/(n0*L)));
sigma_phi=(n0/(A*K))*(beta/(2*n0)+n0^2*alpha*Cphi+((r0*alpha*(n0-1))/(n0*L)));
sigma_average=(Wr+Wphi)/2;

eta=Z(1)/sigma_average      %Efficiency factor.
```

Calculation of the η factor using Method-II.

```
%-------------------------------------------------------
%Calculation of the Efficiency factor, using Method-II
%-------------------------------------------------------

K=0.14;             %Thermal Conductivity
beta=7.3e-6;        %dn/dT Temp. Derivative of index of refraction
alpha=7.5e-6;       %Thermal Coefficient of Expansion
Cr=0.017;           %Photoelastic Coefficient (radial component)
Cphi=-0.0025;       %Photoelastic Coefficient (tangential component)
n0=1.82;            %Index of refraction
r0=0.15;            %Radius of The laser rod
L=6.3;              %Length of the laser rod
%eta_phi            %Efficiency factor (How much is converted to heat when
                    %lasing occurs. Pa=eta*Pin.
                    %Eta is here the overall efficiency factor.

A=pi*r0^2;          %Cross section of the rod.
R0=50;              %Curvature of the end faces of the rod at room temperature
Ip=9.4;             %Threshold current for the diodes.
V=34.1;             %Driver voltage.

%Equation D=sigma*Pa+kappa
kappa=-(2*(n0-1)/R0);

%Currents
I_r=[23.2 22.2 20.3 19.5]; %Values locating Dr.
I_r_eff=I_r-9.4;           %Effective current.
I_phi=[22.8 20.8 20.1];    %Values locating Dphi.
I_phi_eff=I_phi-9.4;       %Effective current.

%Electrical Input Power
Pin_r=V*I_r;               %Input power (radial).
Pin_r_eff=V*I_r_eff;       %Effective input power (radial).

Pin_phi=V*I_phi;           %Input power (azimuthal).
Pin_phi_eff=V*I_phi_eff;   %Effective input power (azimuthal).

f_r=[20 30 40 50];         %Focal lengths (radial).
D_r=1./f_r;                %Refractive power (radial).

f_phi=[30 40 50];          %Focal lengths (azimuthal).
D_phi=1./f_phi;            %Refractive power (azimuthal).

sigma_r=(n0/(A*K))*(beta/(2*n0)+n0^2*alpha*Cr+((r0*alpha*(n0-1))/(n0*L)));
sigma_phi=(n0/(A*K))*(beta/(2*n0)+n0^2*alpha*Cphi+((r0*alpha*(n0-1))/(n0*L)));
```

```
%Data fit.
zphi=polyfit(Pin_phi_eff,D_phi,1); zr=polyfit(Pin_r_eff,D_r,1);

%Efficiency parameters.
eta_phi=zphi(1)/Wphi

eta_r=zr(1)/Wr
```